Serotonergic signaling controls input-specific synaptic plasticity at striatal circuits

Anna Cavaccini[1#], Marta Gritti[1#], Andrea Giorgi[2,7], Andrea Locarno[1], Nicolas Heck[3], Sara Migliarini[2], Alice Bertero[2,7], Maddalena Mereu[4], Giulia Margiani[5], Massimo Trusel[1], Tiziano Catelani[6], Roberto Marotta[6], Maria Antonietta De Luca[5], Jocelyne Caboche[3], Alessandro Gozzi[7], Massimo Pasqualetti[2,7,8] & Raffaella Tonini[1*]

[1]*Neuromodulation of Cortical and Subcortical Circuits Laboratory, Neuroscience and Brain Technologies Department, Istituto Italiano di Tecnologia, Genova, Italy*

[2] *Department of Biology, Unit of Cell and Developmental Biology, University of Pisa, Pisa, Italy*

[3] *Institut de Biologie Paris Seine, Neurosciences Paris Seine, Sorbonne Université, Paris, France*

[4] *Department of Pharmaceutical and Pharmacological Sciences, University of Padua, Padua, Italy*

[5] *Department of Biomedical Sciences, Cittadella Universitaria di Monserrato, University of Cagliari, Cagliari, Italy*

[6] *Electron Microscopy Laboratory, Istituto Italiano di Tecnologia, Genova, Italy*

[7]*Center for Neuroscience and Cognitive Systems, Istituto Italiano di Tecnologia, Rovereto, Italy*

[8]*Neuroscience Institute, National Research Council (CNR), Pisa, Italy*

[#] **Co-first authors**

***Corresponding author**

Raffaella Tonini (raffaella.tonini@iit.it)

Running title

Serotonin controls plasticity at thalamostriatal inputs

Abstract

Monoaminergic modulation of cortical and thalamic inputs to the dorsal striatum (DS) is crucial for reward-based learning and action control. While dopamine has been extensively investigated in this context, the synaptic effects of serotonin (5-HT) have been largely unexplored. Here, we investigated how serotonergic signaling affects associative plasticity at glutamatergic synapses on the striatal projection neurons of the direct pathway (dSPNs). Combining chemogenetic and optogenetic approaches reveals that impeding serotonergic signaling preferentially gates spike-timing-dependent long-term depression (t-LTD) at thalamostriatal synapses. This t-LTD requires dampened activity of the 5-HT4 receptor subtype, which we demonstrate controls dendritic Ca^{2+} signals by regulating BK channel activity, and which preferentially localizes at the dendritic shaft. The synaptic effects of 5-HT signaling at thalamostriatal inputs provide insights into how changes in serotonergic levels associated with behavioral states or pathology affect striatal-dependent processes.

Introduction

The dorsal striatum (DS) of the basal ganglia (BG) plays a critical role in voluntary movement, learning and motivation. It also represents the primary site of dysfunction in psychomotor diseases such as Parkinson's disease (PD), drug addiction and obsessive-compulsive disorders (OCD). The DS receives glutamatergic excitatory inputs from the cortex and thalamus. These inputs converge on striatal projection neurons (SPNs) of the direct (dSPN) and indirect (iSPN) pathways, which exert opposing control over motor output and hedonic states. While dSPNs stimulate movement, reinforcement and reward, iSPNs inhibit movement and mediate punishment and aversion (Kravitz et al., 2010; Kravitz et al., 2012; Tecuapetla et al., 2016; Vicente et al., 2016).

It is increasingly clear that encoding of action selection at striatal circuits requires regulation of SPN activity and plasticity (Kravitz et al., 2012; O'Hare et al., 2016; Sippy et al., 2015). While the neuromodulatory signaling mechanisms controlling iSPN synaptic plasticity, especially long-term-depression (LTD), have been studied extensively, identifying parallel mechanisms in dSPNs has proven more difficult (Zhai et al., 2017). One of the most important neuromodulatory inputs to the striatum is dense dopaminergic innervation from the substantia nigra (Tritsch et al., 2012). In particular, dSPNs expressing the Gs-coupled D1 dopamine (DA) receptors (D1R) are stimulated by dopaminergic signaling. In the presence of behaviorally relevant stimuli, DA is thought to reinforce motor actions that result in reward outcomes through the potentiation of corticostriatal synapses formed on dSPNs. Recent evidence indicates that DA depletion specifically weakens thalamic connections to dSPNs but not to cortical afferents to these neurons (Parker et al., 2016). This weakening, which does not occur in iSPNs, is directly associated with motor abnormalities.

In addition to dopaminergic afferents, serotonergic inputs from the medial and dorsal raphe nucleus (DRN) modulate the activity of SPNs, affecting striatal function and consequently behaviors, including motor and motivational goal-directed behavior (Mathur and Lovinger, 2012). Serotonergic neurons of the DRN fire coincidently with the initiation and termination of selected voluntary movements, whereas reduction in DRN activity to baseline or below is associated with pauses in

motor sequences (Fornal et al., 1996; Jacobs and Fornal, 1999). The evidence that striatal serotonin (5-HT) influences action control is consistent with the dysfunction of the 5-HT system described in OCD and with the use of Selective Serotonin Reuptake Inhibitors (SSRI) for treatment of this disorder (Goddard et al., 2008).

In the DS, 5-HT acts on diverse receptors on both presynaptic and postsynaptic circuit elements (Mathur and Lovinger, 2012). Depending on their localization, striatal 5-HT receptors initiate transduction through several Gi/o-, Gq/11- and Gs protein-dependent and -independent pathways (Hannon and Hoyer, 2008). The specific responses to 5-HT may also be contingent upon cross-talk with other receptor types. In dSPNs, the temporal, combinational logic of serotonergic and D1R-mediated signaling may shape the net synaptic output, depending on the relative balance of these two neuromodulators. It has been reported that increased concentrations of 5-HT in the striatum reduce glutamate release at corticostriatal afferents by activating presynaptic Gi-coupled 5-HT1b receptors (Mathur et al., 2011). 5-HT can also facilitate the release of DA from dopaminergic projections (Navailles and De Deurwaerdere, 2011). Despite their potential implications for BG function and for pathological conditions characterized by hypo-serotonergic states, the synaptic effects of reduced striatal 5-HT signaling remain unexplored. Neither is it known whether there is any input specificity for 5-HT modulation at corticostriatal and thalamostriatal synapses.

In the current study, we investigated the effect of impeding 5-HT release, thereby serotonergic signaling, on timing-dependent synaptic plasticity in dSPNs. This allowed us to describe cellular mechanisms underlying the input-specific impact of 5-HT at thalamostriatal synapses.

Results

Chemogenetic inhibition of 5-HT release gates t-LTD at glutamatergic afferents to dSPNs

To determine how plasticity is modulated at glutamatergic inputs on dSPNs of the dorsolateral striatum (DLS), we recorded excitatory postsynaptic potentials (EPSPs) following intrastriatal stimulation. Intrastriatal stimulation likely activates cortical and thalamic afferents as well as dopaminergic and serotonergic fibers (**Figure 1**)(Shen et al., 2015; Threlfell et al., 2012; Wu et al., 2015). dSPNs were selected through their negative resting membrane potential and firing properties (Kreitzer and Malenka, 2007; Nazzaro et al., 2012). After recording, dSPN cell identity was confirmed by immunostaining for the specific marker substance P, and the lack of immunoreactivity for the iSPN marker A2A (**Figure 1A**) (Nazzaro et al., 2012; Trusel et al., 2015).

We investigated long-lasting changes in EPSPs induced upon a spike-timing-dependent plasticity paradigm (STDP) (Shen et al., 2008). As previously shown (Shen et al., 2008; Shen et al., 2015), a post-pre STDP protocol (**Figure 1B**), in which the postsynaptic spike preceded the presynaptic stimulation, did not induce plasticity in this SPN subpopulation (96 ± 4% of baseline, n = 8, $p > 0.05$; **Figure 1B**). Previous studies show that this STDP protocol leads to long-term synaptic depression (t-LTD) in dSPNs when either D1R are inhibited or striatal DA is depleted (Shen et al., 2008; Shen et al., 2015). The effects of decreased 5-HT signaling at glutamatergic dSPN synapses during STDP remain to be determined, however.

To address the role of 5-HT, we manipulated its release chemogenetically. We used a newly-generated transgenic DREADD (Designer Receptors Exclusively Activated by Designer Drugs) mouse line ($hM4Di^{+/-}$/$Pet1_{210}$-Cre) obtained by crossing the $Pet1_{210}$-Cre transgenic mice (Pelosi et al., 2014) with hM4Di knock-in mice expressing the DREADD hM4Di receptor (hM4DiR) fused in-frame with the mCherry reporter and flanked by two sets of Lox sites (*i.e.*, LoxP/Lox2722) (**Figure S1A**). Upon Cre-mediated somatic recombination, the double-floxed DREADD sequence is effectively inverted, leading to transcription of the inhibitory hM4DiR in $Pet1_{210}$-expressing 5-HT neurons. In brain slices from $hM4Di^{+/-}$/$Pet1_{210}$-Cre mice, these neurons and their projections can be

identified by the expression of the mCherry reporter (**Figure S1B** and **Figure S2A-L**). We first confirmed that the hM4DiR silenced serotonergic neurons of the DRN when activated by its cognate ligand clozapine-N-oxide (CNO; **Figure S1C-F**). Bath application of CNO (5 μM) significantly decreased the firing discharge of $mCherry^{positive}$ but not $mCherry^{negative}$ neurons (**Figure S1D-E**). CNO did not affect the firing rate of DRN 5-HT neurons from $hM4Di^{+/-}$ littermates negative for $Pet1_{210}$-Cre ($Pet1_{210}$-Cre^{0}; **Figure S1F**). mCherry- and 5-HT co-immunoreactivity was verified in the DLS of $hM4Di^{+/-}$/$Pet1_{210}$-Cre mice by immunoelectron microscopy (**Figure S2M-O**). We also confirmed the chemogenetic synaptic silencing of 5-HT release by *in vivo* 5-HT microdialysis in the DLS of freely-moving $hM4Di^{+/-}$/$Petl_{210}$-Cre mice and their control littermates (**Figure S3A**). In $hM4Di^{+/-}$/$Pet1_{210}$-Cre mice, high K^+ (120 mM) infusion in the DLS induced reliable 5-HT release from serotonergic terminals; the stimulatory effect of a second high K^+ challenge was blunted by the intrastriatal infusion of CNO (5 μM; $p < 0.01$; **Figure S3B**). CNO did not affect K^+-evoked release of 5-HT when infused in control mice ($p > 0.05$; **Figure S3C**). These controls indicate that this model can be used to effectively silence the synaptic release of 5-HT in the DLS.

We assessed whether 5-HT synaptic silencing in the DLS affects plasticity outcomes by CNO application in $hM4Di^{+/-}$/$Pet1_{210}$-Cre mice (**Figure 1**). In dSPNs from these mice, t-LTD occurred in the presence of CNO but not in the control (5 μM; 74 ± 4% of baseline, $n = 8$, $p < 0.05$ versus 95 ± 5% of baseline, $n = 5$, $p > 0.05$; **Figure 1C**). There were no changes in synaptic responses when CNO was applied during a burst pattern of back propagating action potentials (bAPs) (94 ± 7% of baseline, $n = 5$, $p > 0.05$) or in the absence of the STDP protocol (93 ± 3% of baseline, $n = 8$, $p > 0.05$; **Figure S4A**). Further, CNO had no effect when applied during the post-pre STDP paradigm in naïve mice (92 ± 6% of baseline, $n = 7$, $p > 0.05$, **Figure S4B**). These results indicate that the chemogenetic inhibition of 5-HT release in the DLS gates t-LTD at glutamatergic afferents to dSPNs.

Antagonism of 5-HT4R signaling enables t-LTD in dSPNs

Our findings indicate that 5-HT, similar to DA through the Gs-coupled D1R (Shen et al., 2008), disrupts the induction of t-LTD in dSPNs. To elucidate the molecular mechanism underlying this role, we tested whether inhibiting 5-HT Gs-mediated signaling allows t-LTD to occur. The striatum contains a high density of the 5-HT6R and 5-HT4R subtypes, which, like D1R, are coupled to Gs, and are expressed in SPNs (Di Matteo et al., 2008). Bath perfusion of the 5-HT6R antagonist SB271046 (5 μM) during the post-pre protocol did not promote plasticity in dSPNs (99 ± 8% of baseline, n = 6, $p > 0.05$, **Figure S4C**). In contrast, delivering the post-pre STDP paradigm in the presence of the 5-HT4R antagonists GR113808 (5 μM) or RS39604 (5 μM) revealed t-LTD in the same neuronal subpopulation (GR113808, 79 ± 5% of baseline, n = 8, $p < 0.05$; RS39604, 68 ± 4% of baseline, n = 10, $p < 0.05$; **Figure 2A**). Thus, 5-HT4R inhibition recapitulates the synaptic effects of chemogenetic inhibition of 5-HT release. Application of either antagonist in the absence of the pairing protocol did not affect glutamatergic synaptic transmission (GR113808, 94 ± 5% of baseline, n = 5, $p > 0.05$; RS39604, 96 ± 4% of baseline, n = 6, $p > 0.05$; **Figure S4D**), confirming that coordinated postsynaptic and presynaptic activity is necessary for the induction of t-LTD.

Previous studies demonstrated that in dSPNs, antagonism of the Gs-coupled D1R signaling allows endocannabinoid (eCB) biosynthesis, ultimately leading to LTD mediated by activation of the presynaptic cannabinoid receptor CB1 (Shen et al., 2008; Shen et al., 2015). However, this was not the putative mechanism for antagonism of 5-HT4R signaling, as the co-application of RS39604 with the CB1R antagonist AM251 (4 μM) did not prevent t-LTD induction (RS39604 + AM251, 62 ± 7% of baseline, n = 5, $p < 0.05$; **Figure 2B**).

We next investigated the locus of plasticity expression by recording synaptic responses generated by twin stimuli, before and after the STDP protocol. In this set of experiments, we found that t-LTD was enabled by antagonism of 5-HT4R (RS39604, 77 ± 5% of baseline, n = 6, $p < 0.05$; **Figure 2C**), but was not accompanied by a change in paired-pulse-ratio (PPR), a hallmark of presynaptic plasticity (PPR: $before_{STDP}$, 1.33 ± 0.09; $after_{STDP}$, 1.36 ± 0.10, $p > 0.05$; **Figure 2C**).

This raises the possibility that this form of LTD is expressed postsynaptically. Consistent with this, intracellular dialysis of the peptide D15 (1.5 mM) – a peptide that prevents AMPAR endocytosis by disrupting the interaction between dynamin and amphiphysin (Carroll et al., 1999; Morishita et al., 2005) – blocked t-LTD (D15/RS39604, 91 ± 5% of baseline, n = 8, $p > 0.05$), whereas dialysis of a scramble peptide (S15, 1.5 mM) had no effect (S15/RS39604, 63 ± 8% of baseline, n = 5, $p < 0.05$; **Figure 2D**). The application in the postsynaptic neuron of the $GluA2_{3Y}$ peptide (100 μg/ml), which blocks regulated, but not constitutive, AMPAR endocytosis (Brebner et al., 2005; Collingridge et al., 2010) had a similar effect ($GluA2_{3Y}$/RS39604, 94 ± 3% of baseline, n = 6, $p > 0.05$; **Figure 2D**). Confirming this peptide's specific action, the control peptide $GluA2_{3A}$ (100 μg/ml) did not influence plasticity ($GluA2_{3A}$/RS39604, 70 ± 5% of baseline, n = 6, $p < 0.05$; **Figure 2D**). Furthermore, variance analysis of synaptic responses indicated that t-LTD resulting from chemogenetic inhibition of 5-HT release (**Figure 1**) or application of 5-HT4R antagonists (**Figure 2**) is not accompanied by changes in trial-to-trial variation in EPSP amplitude (**Figure S4E**). This further supports a postsynaptic locus of plasticity expression (Shen et al., 2008).

Overall, these data indicate that 5-HT controls plasticity induction in dSPNs through the activation of 5-HT4R; this effect is not mediated by eCBs and it relies on postsynaptic expression mechanisms.

Serotonin modulates bAP-induced Ca^{2+} transients during STDP

At glutamatergic synapses on SPNs, the induction of t-LTD depends on the temporal convergence of synaptic input and postsynaptic elevations of dendritic Ca^{2+} signal triggered by bAPs (Plotkin et al., 2013; Shindou et al., 2011). 5-HT has been shown to regulate ionic conductance that may affect the propagation of bAPs (King et al., 2008). Modulation of the bAP-induced Ca^{2+} signal may therefore be one of the mechanisms that affect timing-dependent synaptic plasticity in dSPNs (Plotkin et al., 2013; Shindou et al., 2011; Zhou et al., 2005). To test this hypothesis, simultaneously with the chemogenetic and pharmacological inhibition of 5-HT signaling, we performed two-photon

Ca^{2+} imaging and whole-cell current clamp recordings and monitored changes in intracellular Ca^{2+}. In the proximal dendrites of dSPNs, a single bout of the negative STDP protocol (1b-STDP) triggered Ca^{2+} transients that were stable over time, as indicated by the lack of variation in the area under the curve (AUC) of the fluorescence transients over 10 to 15 min (106 ± 8% of control; n = 8, $p > 0.05$; **Figure 3A**). In the dSPNs of $hM4Di^{+/-}/Pet1_{210}$-Cre mice, bath application of CNO (5 μM) to impede 5-HT release enhanced dendritic Ca^{2+} influx in response to 1b-STDP (AUC, 130 ± 8% of control; n = 11, $p < 0.01$; **Figure 3B**). The 1b-STDP-associated dendritic Ca^{2+} signal increased upon application of the two 5-HT4R antagonists GR113808 (5 μM; AUC, 122 ± 6% of control; n = 15, $p < 0.01$; **Figure 3C**) or RS39604 (5 μM; AUC, 130 ± 7% of control; n = 14, $p < 0.01$; **Figure 3C**). Together, these results indicate that impeding 5-HT4R-mediated signaling boosts the bAP-induced dendritic Ca^{2+} signal.

These results appear to conflict with the notion that activation, not inhibition, of Gs-coupled receptors typically enhances voltage-gated Ca^{2+} currents triggered by APs via stimulation of protein kinase A (PKA) (Higley and Sabatini, 2010). In several neuronal subtypes, including striatal SPNs, inhibition of various types of K^+ currents that contribute to the AP repolarization, and after hyperpolarization phases, enhances dendritic Ca^{2+} transients (Cai et al., 2004; Day et al., 2008; Trusel et al., 2015). Therefore, we hypothesized that 5-HT4R regulates dendritic Ca^{2+} levels by instead influencing the activity of K^+ channels. In addition to PKA, 5-HT4R can potentially signal to Ca^{2+}/calmodulin-dependent protein kinase II (CaMKII) (Liu and Voyno-Yasenetskaya, 2005; Ponimaskin et al., 2002), which positively regulates the activity of the large-conductance Ca^{2+}-activated K^+ channel BK (Nelson et al., 2005; van Welie and du Lac, 2011). To test if this is the case in dSPNs, we applied the BK channel blocker paxilline (10 μM) to isolate the BK-mediated current (as the paxilline-sensitive component, $I_{Paxilline}$) in response to a depolarizing voltage-ramp protocol (**Figure S5A**) (Deng et al., 2013). The 5-HT4R agonist RS67333 (5 μM) significantly enhanced $I_{paxilline}$ amplitude ($p < 0.05$); this effect was prevented by the postsynaptic intracellular application of

a specific competitive inhibitor of CaMKII, the Autocamtide-2-Related Inhibitory Peptide (AIP, 10 μM; $p > 0.05$; **Figure S5B**). We also confirmed that stimulating 5-HT4R activates CaMKII in DLS dSPNs. On acute striatal slices from drd1a-tdTomato^{tg} mice, which express Tomato in dSPNs (Shuen et al., 2008), we monitored phosphorylation of CaMKII at Thr286 (pCaMKII). Incubation (10 min) with the 5-HT4R agonist RS67333 (5 μM) significantly increased the number of pCaMKII^{+}/Tomato^{+} cells compared to controls ($p < 0.01$; **Figure S5C**). These data indicate that 5-HT4R can signal through CaMKII to positively modulate BK channel activity in dSPNs.

BK channels shape the duration of bAP in several neuronal populations and affect dendritic Ca^{2+} influx (Golding et al., 1999). Therefore, reduced release of 5-HT or direct inhibition of 5-HT4R could dampen the activation of BK channels during the STDP protocol, leading to an enhanced dendritic Ca^{2+} signal in response to bAPs. To test this, we first assessed whether blocking BK channels occluded the effect of RS39604. Bath perfusion of paxilline (10 μM) significantly enhanced the 1b-STDP-associated Ca^{2+} transient (AUC, 138 ± 7% of control; $n = 9$, $p < 0.001$; **Figure 3D**). As predicted, sequential co-application of paxilline with RS39604 had no further effect on the induced change in dendritic fluorescence (AUC, 139 ± 7% of control; $p < 0.001$; 100 ± 3% of paxilline, $p > 0.05$; $n = 9$; **Figure 3D**), suggesting that BK channels are targets of 5-HT4R signaling.

5-HT4R modulates bAP-induced Ca^{2+} signal through CaMKII

Our 1b-STDP-stimulation protocol is likely to activate a set of glutamatergic, dopaminergic and serotonergic inputs. Thus, it cannot isolate the impact of 5-HT4R on dendritic Ca^{2+} influx specifically induced by bAPs. To overcome this issue, we estimated the Ca^{2+} transients generated by somatically eliciting postsynaptic bAPs in the absence of presynaptic stimulation (**Figure 3E**). We replaced the contribution of 5-HT release on local electrical stimulation with the direct pharmacological stimulation of 5-HT4R by the agonist RS67333 (5 μM). Consistent with the hypothesis that 5-HT4R stimulate a K^{+} channel conductance, the presence of RS67333 reduced the

bAP-induced Ca^{2+} signal (AUC, 71 ± 7% of control; n = 10, $p < 0.01$; **Figure 3E**). Furthermore, blocking BK-mediated current prevented the effect of 5-HT4R stimulation: RS67333 failed to reduce the bAP-induced Ca^{2+} transients upon pre-exposure to paxilline (AUC, paxilline, 142 ± 10% of control; $p < 0.01$; paxilline + RS67333, 142 ± 9% of control, $p < 0.05$; paxilline + RS67333, 101 ± 7% of paxilline, $p > 0.05$; n = 7; **Figure 3F**). Further, the intracellular application of the CaMKII inhibitor AIP (10 μM) prevented RS67333 from reducing Ca^{2+} transients elicited by bAPs (AUC, 105 ± 5% of AIP, $p > 0.05$; n = 10; **Figure 3G**). The selective cell-permeable CaMKII inhibitor KN-62 (10 μM) had a similar effect: bath application boosted bAP-induced Ca^{2+} transients (**Figure S5D**). This is consistent with bursts of bAPs activating CaMKII in proximal dendrites (Lee et al., 2009), and with CaMKII hindering the activation of BK channels recruited by bursts of bAPs, thus resulting in enhanced Ca^{2+} transients. KN-62 prevented the inhibitory effect of RS67333 (AUC, KN-62, 155 ± 15% of control, $p < 0.05$; KN-62 + RS67333, 158 ± 22% of control, $p < 0.05$; KN-62 + RS67333, 99 ± 7% of KN-62, $p > 0.05$; n = 7, **Figure S5D**), further supporting that CaMKII acts downstream of 5-HT4R to regulate bAP-induced Ca^{2+} transients.

These results indicate that the modulatory effect of 5-HT4R activation involves CaMKII signaling. PKA may also act in the same pathway to shape bAP-induced Ca^{2+} signal. Nevertheless, when the PKA inhibitor peptide 5-24 (20 μM) was intracellularly applied, RS67333 still reduced bAP-induced Ca^{2+} signal (AUC: 83 ± 5% of PKI; $p < 0.05$, n = 7; **Figure S5E**), suggesting PKA does not play a major role in this process.

Overall, these data indicate that regulation of BK channel activity is required for the 5-HT4R-mediated modulation of dendritic Ca^{2+} signal in dSPNs, and this modulation involves CaMKII signaling.

5-HT4R-mediated signaling does not modulate plasticity at cortico-dSPN synapses

We have demonstrated that 5-HT signaling, through the 5-HT4R subtype, influences the postsynaptic response of dSPNs to glutamatergic input activation during STDP. To dissect whether this modulation occurs at cortical and/or thalamic inputs, we probed the striatal circuitry with optogenetics. First, we used Thy1-ChR2 transgenic mice to measure postsynaptic responses evoked by light activation of corticostriatal afferents, which represent at least 50% of glutamatergic synapses on SPNs (Doig et al., 2010; Huerta-Ocampo et al., 2014). In these mice, the expression of channel rhodopsin (ChR2) is high in cortical layer V neurons (**Figure 4A**) and appears not to extend to thalamostriatal neurons (Plotkin et al., 2014; Wu et al., 2015). Short blue light pulses through the microscope objective (0.1-1 ms at 470 nm) elicits EPSPs in dSPNs (o-$EPSP_{Ctx}$). We investigated post-pre STDP at corticostriatal synapses by monitoring o-$EPSP_{Ctx}$ before and after the induction protocol. During the post-pre pairing paradigm, optogenetic stimulation of cortical inputs was replaced by conventional electrical stimulation in order to recruit 5-HT fibers (**Figure 4B**). In this experimental setting, the STDP protocol failed to induce significant changes in o-$EPSP_{Ctx}$ (98 ± 8% of baseline, n = 7, $p > 0.05$; **Figure 4C**), even when applied in the presence of RS39604 (5μM; 92 ± 6% of baseline, n = 8, $p > 0.05$; **Figure 4C**). To corroborate this lack of involvement of corticostriatal synapses in a second model, we injected an adeno-associated viral (AAV) vector encoding ChR2-eYFP under the control of the CaMKIIa promoter [rAAV5-CaMKIIa-ChR2(H134R)-eYFP] into the M1 motor cortex region of C57BL/6J mice (Johnson et al., 2017) (**Figure S6A**). As with Thy1-ChR2 mice (**Figure 4C**), the STDP protocols failed to induce significant changes in dSPNs o-$EPSP_{Ctx}$, regardless of the presence or absence of RS39604 ($dSPN_{Ctx}$, 97 ± 6% of baseline, n = 7, $p > 0.05$; $dSPN_{Ctx}$ + RS39604, 90 ± 2% of baseline, n=6, $p > 0.05$; $dSPN_{Ctx}$ versus $dSPN_{Ctx}$ + RS39604, $p = 0.7$ Mann Whitney test; **Figure S6B-C**). Thus, corticostriatal synapses are not the primary target of the 5-HT4R-mediated effects at non-dissected glutamatergic inputs to dSPNs (**Figure 2A**).

5-HT signaling controls t-LTD at thalamic inputs

The results described to this point suggest that gating of t-LTD due to decreased 5-HT signaling is in fact occurring at thalamostriatal inputs. To test this, we virally expressed ChR2 in the thalamus of C57BL/6J mice (**Figure 4D**) (Ellender et al., 2013; Johnson et al., 2017), and measured light-evoked EPSPs (o-$EPSP_{Thal}$) at thalamostriatal connections. To induce plasticity, we applied the same post-pre STDP paradigm described for corticostriatal synapses (**Figure 4B**). As predicted, the STDP protocol did not evoke plasticity of o-$EPSP_{Thal}$ in dSPNs under control conditions (103 ± 10% of baseline, n = 6, $p > 0.05$; **Figure 4E**), whereas it triggered a significant t-LTD of o-$EPSP_{Thal}$ in the presence of RS39604 (5μM; 71 ± 8% of baseline, n = 8, $p < 0.05$, **Figure 4E**). We also controlled for the cell-type specificity of this effect. In iSPNs, the post-pre STDP paradigm already induced t-LTD of o-$EPSP_{Thal}$ in control conditions (o-$EPSP_{Thal}$, 67 ± 5% of baseline, n = 7, $p < 0.05$; **Figure S7A-B**); the application of RS39604 did not influence the plasticity outcome (o-$EPSP_{Thal}$ + RS39604, 68 ± 8% of baseline, n = 5, $p < 0.05$; **Figure S7B**).

We next assessed the link between the synaptic effects of 5-HT at thalamic inputs with the regulation of BK channel activity (**Figure 3**). In our model, decreased 5-HT signaling dampens the activation of BK channels during STDP and boosts the Ca^{2+} signal induced by bAP (**Figure 3**). This mechanism could underlie the permissive role of 5-HT4R inhibition on t-LTD induction (**Figure 2A** and **Figure 4E**). If this is the case, we would expect the pharmacological inhibition of BK channels during conventional STDP to be sufficient to gate synaptic depression at thalamic inputs recruited by optogenetic activation. Reminiscent of 5-HT4R antagonism and chemogenetic inhibition of 5-HT release, in the presence of the BK channel blocker paxilline (10 μM), the STDP paradigm resulted in t-LTD of o-$EPSP_{Thal}$ (75 ± 4 % of baseline, n = 7, $p < 0.05$, **Figure S8A**).

The $hM4Di^{+/-}$/$Pet1_{210}$-Cre animals expressing ChR2 in the thalamus showed similar effects (**Figure 4F**) as those described above. The chemogenetic inhibition of 5-HT release by bath application of CNO (5 μM) during the post-pre STDP paradigm enabled t-LTD at thalamo-dSPN synapses ($dSPN_{DREADD\_Thal,}$ 93 ± 1 % of baseline, n = 7, $p > 0.05$; $dSPN_{DREADD\_Thal,}$ + CNO, 61 ± 5 %

of baseline, n = 7, $p < 0.05$; **Figure 4F**). Together, these results indicate that impeding serotonergic signaling, and in turn the activation of the 5-HT4R subtype, is sufficient to gate t-LTD at thalamostriatal synapses.

In addition to bAP-induced Ca^{2+} transients, NMDA receptor activation is a possible means by which dendritic Ca^{2+} signals could be enhanced to enable t-LTD at thalamostriatal synapses on dSPNs (Ellender et al., 2013; Wu et al., 2015). However, the NMDAR antagonist R-CPP (10 μM) had no effect on o-$EPSP_{Thal}$ t-LTD gated by inhibition of BK channels during the post-pre STDP paradigm ($dSPN_{Thal}$ + Paxilline + R-CPP, 78 ± 6% of baseline, n = 7, $p < 0.05$; **Figure S8A**) or by chemogenetic inhibition of 5-HT release in $hM4Di^{+/-}$/$Pet1_{210}$-Cre mice ($dSPN_{DREADD\_Thal,}$ + CNO + R-CPP, 60 ± 7% of baseline, n = 5, $p < 0.05$; **Figure S8B**). This indicates that NMDARs are not involved in this form of synaptic depression.

Lastly, we asked whether activating 5-HT4R signaling during the post-pre STDP paradigm is sufficient to disrupt t-LTD at thalamic inputs to dSPNs. We first tested the assumption that t-LTD at thalamo-dSPN synapses is suppressed by neuromodulatory signals (including 5-HT) released upon conventional electrical stimulation during STDP, as previously proposed (Wu et al., 2015). We re-examined plasticity of o-$EPSP_{Thal}$ upon the delivery of an optogenetic post-pre pairing STDP protocol (o-STDP), which exclusively engages thalamic afferents. In this experimental setting, we observed a form of t-LTD at thalamo-dSPN synapses (72 ± 6% of baseline, n = 6, $p < 0.05$, **Figure 5A**), consistent with previous observations (Ellender et al., 2013; Wu et al., 2015). The 5-HT4R agonist RS67333 (5 μM) prevented t-LTD of o-$EPSP_{Thal}$ when applied during the o-STDP paradigm (91 ± 3 % of baseline, n = 8, $p < 0.05$; **Figure 5A**). We also injected the rAAV5-EF1a-DIO-hChR2(H134R)-eYFP virus into the DRN of $Petl_{210}$-Cre mice to exert an optogenetic control of 5-HT release during plasticity induction (**Figure 5B**). In oblique horizontal slices from these mice, we electrically elicited thalamic synaptic responses in the DLS (e-$EPSP_{Thal}$) by placing the stimulating electrode in the thalamus, close to the border of the thalamic reticular nucleus (**Figure 5C**) (Ding et al., 2008; Ding et al., 2010). Consistent with the response to the o-STDP paradigm (**Figure 5A**), e-$EPSP_{Thal}$ showed

t-LTD upon a post-pre STDP paradigm in which thalamic axons were stimulated (Thal-STDP) (61 ± 7% of baseline, n = 6, $p < 0.05$; **Figure 5C-D**). Optogenetically evoking 5-HT release at the time of presynaptic stimulation during pairing prevented t-LTD of e-$EPSP_{Thal}$ (93 ± 5% of baseline, n = 8, $p > 0.05$); plasticity was rescued by the application of RS39604 (5 μM; 44 ± 7% of baseline, n = 5, $p < 0.05$; **Figure 5C-D**). This also indicates that t-LTD suppression is not due to light-induced release of glutamate from DRN terminals.

Collectively, these results further support the involvement of the 5-HT4R subtype in the 5-HT-mediated modulation of t-LTD at thalamic inputs on dSPNs.

5-HT4R preferentially localizes at thalamostriatal synapses

To increase certainty of the input specificity of the 5-HT4R mediated effects, we combined immunohistochemistry with three-dimensional (3D) segmentation and morphometric analysis of glutamatergic DLS synapses (Gilles et al., 2017) (**Figure 6** and **Figure S9A-B**). We initially monitored the expression of 5-HT4R in two different mouse lines: the VGLUT1-Venus knock-in line, which expresses the VGLUT1 transporter fused to the YFP-variant Venus, and which allows direct visualization of axonal boutons from cortical afferents (Heck et al., 2015; Herzog et al., 2004); and the VGLUT2-Cre transgenic mice injected in the thalamus with the AAVrh9-pCAG-flex-eGFP-WRPE virus (AAV-FLEX-eGFP), to visualize thalamic inputs to the striatum. In this second mouse line, thalamic boutons were identified by immunolabeling for the presynaptic marker Bassoon (Sudhof, 2012). We measured the 3D edge-to-edge minimal distance from VGLUT1-positive cortical boutons and VGLUT2-positive thalamic boutons to the closest 5-HT4R. Although there was a higher density of VGLUT1 boutons, the distance between VGLUT1 boutons and 5-HT4R was significantly greater than between VGLUT2 boutons and 5-HT4R (VGLUT1-5-HT4R, 608 ± 26 nm; VGLUT2-5-HT4R, 364 ± 19 nm, $p < 0.0001$; with 19.34 ± 1.23 VGLUT2 co-localizing with 5-HT4R and 9.81 ± 0.74 VGLUT1 co-localizing with 5-HT4R; **Figure 6A**). These morphological data support our

functional observations showing that thalamostriatal synapses are the primary site of 5-HT4R-mediated effects (**Figure 4**).

We then investigated the postsynaptic subcellular localization of 5-HT4R in dSPNs. The viral construct AAVrh9-PPTA-Cre (AAV-PPTA-Cre), which contains an expression cassette consisting of Cre recombinase driven by the dSPN-specific promoter of the PPTA gene (substance P), and the AAVrh9-pCAG-flex-tdTomato-WRPE (AAV-FLEX-tdTOMATO) construct expressing "flexed" tdTomato (Dos Santos et al., 2017; Hikida et al., 2010; Yagishita et al., 2014) were co-injected into the DLS. In dSPNs, we measured the number of co-localizing 5-HT4Rs in 3D-reconstructed dendrites and segmented headspines. 5-HT4R localization is predominant in the shaft, with 3.2 ± 0.5 5-HT4R per 10 μm of dendritic length (**Figure 6B**). To selectively visualize thalamic terminals on dSPNs, we analyzed VGLUT2-Cre mice co-injected with the AAV-FLEX-eGFP virus in the thalamus and with the AAV-PPTA-Cre and the AAV-FLEX-dtTOMATO viruses in the DLS. This analysis confirmed the postsynaptic subcellular localization of 5-HT4R in both axo-spinous and axo-dendritic thalamostriatal synapses (**Figure 6C**).

Discussion

The results presented here reveal a previously unknown role of 5-HT at striatal circuits. This is the first demonstration that signaling by 5-HT receptors provides a control mechanism of Hebbian plasticity (t-LTD) at thalamo-SPN synapses of the direct pathway. These synaptic effects of 5-HT are mediated by the postsynaptic 5-HT4R subtype, which shapes bAP-evoked dendritic Ca^{2+} signals through the regulation of BK channel activity, and which is preferentially localized at axo-dendritic thalamostriatal synapses.

Our findings help elucidate the full complement of 5-HT actions in the dorsal striatum. Previous observations have shown that increasing 5-HT levels in the DLS reduces presynaptic glutamate release and depresses neurotransmission at corticostriatal inputs through the activation of the presynaptic 5-HT1b receptor (Mathur et al., 2011). Notably, 5-HT1b-mRNA is detectable in layer V cortical neurons, but not in the thalamic intralaminar nuclei (Allen Brain Atlas; http://www.brain-map.org/). In the current study, we find that impeding serotonergic signaling, thereby dampening the activation of the 5-HT4R subtype, affects postsynaptic dendritic Ca^{2+} signals and gates spike-timing-dependent long-term depression (t-LTD) preferentially at thalamic afferents to dSPNs.

Results presented in this study and by Mathur et al. (2011) highlight the complexity of striatal 5-HT signaling, which acts through diverse receptors at both presynaptic and postsynaptic sites (Mathur and Lovinger, 2012), and which may show specific subcellular compartmentalization. Here, we provide evidence that 5-HT4Rs are enriched at thalamostriatal synapses compared to cortical ones, and primarily localize at the dendritic shaft. Exogenously applied 5-HT or inhibition of 5-HT reuptake depresses corticostriatal afferents, whereas decreased synaptic release of 5-HT during STDP gates t-LTD at thalamostriatal inputs, suggesting that the net synaptic effect of 5-HT likely depends on its spatiotemporal dynamic in response to different patterns of stimulation. This may ultimately lead to spatiotemporal specificity of synaptic plasticity at defined inputs (i.e., cortical and thalamic inputs).

Upon impeding 5-HT signaling, t-LTD at undissected glutamatergic inputs is of an only slightly lower magnitude than that at thalamostriatal inputs recruited by optogenetic activation. These

results appear to be at odds with the notion that at least 50% of excitatory inputs to SPNs are from the cortex (Doig et al., 2010; Huerta-Ocampo et al., 2014), and our current finding that inhibiting 5-HT4R does not gate plasticity at corticostriatal synapses. Indeed, one might predict that the magnitude of LTD recorded during electrical stimulation experiments would be algebraically diluted by unaffected cortical synapses. This prediction would require the plasticity at cortical and thalamic inputs to be independent. However, we cannot exclude that the Ca^{2+} influx at cortical synapses that respond to electrical stimulation might influence thalamic synapses during the post-pre STDP. Although cortical synapses do not experience t-LTD upon 5-HT4R inhibition, Ca^{2+}-activated signaling molecules might diffuse from cortical spines to the dendritic shaft (Tang and Yasuda, 2017), where 5-HT4Rs strongly co-localize with thalamic inputs (this study). This might affect local dendritic spikes and facilitate cooperative plasticity at thalamostriatal synapses (Golding et al., 2002; Popescu et al., 2007). An alternative scenario is that electrical stimulation may activate unidentified inputs contributing to the EPSP that also experience LTD upon inhibition of 5-HT signaling; this form of plasticity might be independent of that occurring at thalamostriatal inputs.

Our findings add to the limited knowledge of the intracellular signaling pathways regulating the thalamostriatal system, in particular the molecular mechanisms underlying synaptic depression of thalamo-dSPN synapses (Atwood et al., 2014; Ellender et al., 2011; Johnson et al., 2017; Parker et al., 2016; Wu et al., 2015). t-LTD at thalamostriatal inputs has been shown to be independent of eCBs released from the postsynaptic SPN (Wu et al., 2015). Consistent with this and with the evidence that thalamic afferents to the striatum are devoid of presynaptic CB1R (Wu et al., 2015), we found that t-LTD gated by 5-HT4R antagonism is insensitive to CB1R inhibition, and relies on postsynaptic expression mechanisms. In the DS, 5-HT4Rs are localized mainly postsynaptically (Di Matteo et al., 2008). Activation of this Gs-coupled receptor subtype typically increases PKA activity and leads to the inhibition of K^+ channels (King et al., 2008). Our findings point to an alternative signaling mechanism which involves CaMKII and activation of large-conductance BK channels. Indeed, 5-HT4R can couple not only with Gs proteins, but also with Gα13, which signals to CaMKII (Liu and

Voyno-Yasenetskaya, 2005; Nelson et al., 2005; Ponimaskin et al., 2002). In brain regions other than the striatum, CaMKII positively regulates BK channels (Nelson et al., 2005; Smith et al., 2002). We found that the paxilline-sensitive, BK channel-mediated current was significantly increased upon 5-HT4R activation, and this enhancement was prevented by inhibition of CaMKII. The most parsimonious interpretation of these results is that 5-HT4R activation leads to CaMKII activation, which, in turn, increases the amplitude of the BK channel-mediated current.

The post-pre STDP protocol used in this study (intrastriatal stimulation) may be reminiscent of behavioral states in which the striatal release of 5-HT (and other neuromodulators) occurs concomitantly with coordinated post- and presynaptic activity. In post-pre STDP, the EPSP coincides with the afterhyperpolarization (AHP) that follows the bAP (Feldman, 2012). Ultimately affecting bAP-induced Ca^{2+} transients, AHP is shaped by the activity of Ca^{2+}-activated K^+ conductances, including BK channels (Day et al., 2008). We propose a model in which 5-HT positively modulates BK channel activity via stimulation of 5-HT4R during the post-pre STDP paradigm, ultimately reducing dendritic bAP-induced Ca^{2+} influx (**Figure 7**). This may hinder the induction of t-LTD at thalamo-dSPN synapses, possibly by interfering with signaling pathways involved in the internalization of AMPAR (Grueter et al., 2010; Luscher et al., 2000).

Conversely in this model, a decrease in 5-HT signaling during conventional post-pre STDP would dampen activation of BK channels and enhance bAP-induced Ca^{2+} signaling, thus promoting AMPAR internalization and enabling t-LTD (Grueter et al., 2010; Luscher et al., 2000) (**Figure 7**). This could potentially mimic the circumstances in vivo, *e.g.*, when post-pre STDP is uncorrelated to 5-HT release but occurs concomitantly with dopamine release or when there are pathological conditions characterized by hypofunctioning of the serotonergic system. Although our findings do not establish the precise identity of the thalamic afferents that are modulated by 5-HT, only thalamic inputs from the parafascicular thalamic (Pf) nucleus, and not from the central lateral (CL) nucleus, have been shown to express t-LTD (Ellender et al., 2013). Notably, Pf nucleus projections are the primarily source for axo-dendritic synapses on SPNs (Smith et al., 2014), where we found 5-HT4R

to primarily localize, at least on dSPNs.

The 5-HT-mediated regulation of dendritic Ca^{2+} signaling during STDP represents a means by which changes in serotonergic levels may shape the thalamostriatal system. Projections of the intralaminar nuclei of the thalamus to the striatum are critical to interrupt ongoing motor behavior and redirect attention toward salient stimuli (Thorn and Graybiel, 2010), or to encoding A-O contingencies (Bradfield et al., 2013a; Bradfield et al., 2013b). Therefore, gating mechanisms of t-LTD at thalamic inputs that depend on serotonergic levels may affect the BG network and striatal information processing. Investigating the behavioral impact of 5-HT signaling specifically through the 5-HT4R subtype, as well as establishing synaptic causalities with modulation of thalamostriatal inputs, is certaintly an area for future studies.

Our results indicate that 5-HT at thalamic inputs, via 5-HT4R, exert a similar function as DA at cortical inputs, via D1R (Shen et al., 2008); both signaling pathways contribute to the activation of dSPNs by increasing the strength of glutamatergic inputs. The fact that the activation of D1R by DA released during intrastriatal stimulation (Shen et al., 2015; Threlfell et al., 2012; Wu et al., 2015) cannot compensate for the decrease in Gs signaling when 5-HT4Rs are blocked suggests that D1R and 5-HT4R may be localized in the different functional microdomains. Further studies are required to assess whether D1Rs segregate at cortical spines. Regardless, morphologically, 5-HT4Rs are predominately localized at axo-dendritic rather than axo-spinous synapses. Since only thalamic inputs, but not cortical afferents, form axo-dendritic synapses, this subcellular postsynaptic localization of 5-HT4R (**Figure 6**) is consistent with the effects of 5-HT being specific to thalamic inputs. Building on existing models of striatal plasticity, we may now recognize excitatory DA and 5-HT as two complementary neuromodulatory systems controlling timing-dependent plasticity at two different glutamatergic inputs to dSPNs. This might allow for greater selectivity in tuning the activity of the direct pathway, which supports reinforcement and reward (Fisher et al., 2017; Kravitz et al., 2012).

Overall, the findings from this study not only provide mechanistic insights into the thalamic

control of striatal functions, but they also identify synaptic substrates for maladaptive plasticity in BG disorders that involve dysfunction of the serotonergic system.

Acknowledgments

We are grateful to Mattia Pesce and Alice Gino for technical assistance during imaging experiments and immunohistochemistry, and to Alexis Bemelmans (Molecular Imaging Research Center, Commissariat pour l'Energie Atomique, France) for producing the adeno-associated virus PPTA-Cre. This research was primarly supported by the Fondazione Istituto Italiano di Tecnologia (to RT) and by grants provided by Compagnia di San Paolo (# 2013 0942 to RT) and Fondazione Cariplo (# 2013 0871 to RT). J.C./N.H. were supported by the Centre National pour la Recherche Scientifique (CNRS), Sorbonne University, the Fondation pour la Recherche Médicale (# DEQ20150734352 to J.C.) and the Labex Bio-Psy Cluster of Excellence; A. Go acknowledges the Brain and Behavior Foundation (2017 NARSAD independent Investigator Grant) and the Simons Foundation (SFARI 400101).

Author contributions

A.C and M.G. designed, performed and analyzed the electrophysiological experiments. M.G. conducted and analyzed the imaging experiments A.Gi., M.P. and A.Go. designed and generated the hM4Di$^{+/-}$/Pet1$_{210}$-Cre mouse line. A.L. conducted and analyzed some electrophysiological recordings. M.G., A.Gi., M.T, A.L. and A.B. performed intracerebral viral injections. A.C., M.G. and M.T. performed immunostaining to identify dSPNs and iSPNs. S.M. and A.B. carried out the immunofluorescence analyses. M.M., G.M. and M.DeL. performed microdialysis in mice. N.H. carried out the 3D morphometric analysis with the help of M.G. N.H. and J.C. conducted the immunohistochemical analysis on acute brain slices. T.C. and R.M. performed the electron microscopy analysis. A.C., M.G., A.L. and M.P. contributed to critical reading of the manuscript. M.P supervised A.Gi, S.M. and A.B.; R.T. conceived the study, supervised the project, directed the experiments and wrote the manuscript.

Competing financial interests

The authors declare no competing financial interests.

References

Atwood, B.K., Kupferschmidt, D.A., and Lovinger, D.M. (2014). Opioids induce dissociable forms of long-term depression of excitatory inputs to the dorsal striatum. Nature neuroscience 17, 540-548.

Bradfield, L.A., Bertran-Gonzalez, J., Chieng, B., and Balleine, B.W. (2013a). The thalamostriatal pathway and cholinergic control of goal-directed action: interlacing new with existing learning in the striatum. Neuron 79, 153-166.

Bradfield, L.A., Hart, G., and Balleine, B.W. (2013b). The role of the anterior, mediodorsal, and parafascicular thalamus in instrumental conditioning. Frontiers in systems neuroscience 7, 51.

Brebner, K., Wong, T.P., Liu, L., Liu, Y., Campsall, P., Gray, S., Phelps, L., Phillips, A.G., and Wang, Y.T. (2005). Nucleus accumbens long-term depression and the expression of behavioral sensitization. Science 310, 1340-1343.

Cai, X., Liang, C.W., Muralidharan, S., Kao, J.P., Tang, C.M., and Thompson, S.M. (2004). Unique roles of SK and Kv4.2 potassium channels in dendritic integration. Neuron 44, 351-364.

Carroll, R.C., Beattie, E.C., Xia, H., Luscher, C., Altschuler, Y., Nicoll, R.A., Malenka, R.C., and von Zastrow, M. (1999). Dynamin-dependent endocytosis of ionotropic glutamate receptors. Proc Natl Acad Sci U S A 96, 14112-14117.

Clarke, H.F., Dalley, J.W., Crofts, H.S., Robbins, T.W., and Roberts, A.C. (2004). Cognitive inflexibility after prefrontal serotonin depletion. Science 304, 878-880.

Collingridge, G.L., Peineau, S., Howland, J.G., and Wang, Y.T. (2010). Long-term depression in the CNS. Nat Rev Neurosci 11, 459-473.

Day, M., Wokosin, D., Plotkin, J.L., Tian, X., and Surmeier, D.J. (2008). Differential excitability and modulation of striatal medium spiny neuron dendrites. J Neurosci 28, 11603-11614.

Deng, P.Y., Rotman, Z., Blundon, J.A., Cho, Y., Cui, J., Cavalli, V., Zakharenko, S.S., and Klyachko, V.A. (2013). FMRP regulates neurotransmitter release and synaptic information transmission by modulating action potential duration via BK channels. Neuron 77, 696-711.

Di Matteo, V., Pierucci, M., Esposito, E., Crescimanno, G., Benigno, A., and Di Giovanni, G. (2008). Serotonin modulation of the basal ganglia circuitry: therapeutic implication for Parkinson's disease and other motor disorders. Prog Brain Res 172, 423-463.

Ding, J., Peterson, J.D., and Surmeier, D.J. (2008). Corticostriatal and thalamostriatal synapses have distinctive properties. J Neurosci 28, 6483-6492.

Ding, J.B., Guzman, J.N., Peterson, J.D., Goldberg, J.A., and Surmeier, D.J. (2010). Thalamic gating of corticostriatal signaling by cholinergic interneurons. Neuron 67, 294-307.

Doig, N.M., Moss, J., and Bolam, J.P. (2010). Cortical and thalamic innervation of direct and indirect pathway medium-sized spiny neurons in mouse striatum. J Neurosci 30, 14610-14618.

Dos Santos, M., Cahill, E.N., Bo, G.D., Vanhoutte, P., Caboche, J., Giros, B., and Heck, N. (2017). Cocaine increases dopaminergic connectivity in the nucleus accumbens. Brain Struct Funct.

Ellender, T.J., Harwood, J., Kosillo, P., Capogna, M., and Bolam, J.P. (2013). Heterogeneous properties of central lateral and parafascicular thalamic synapses in the striatum. J Physiol 591, 257-272.

Ellender, T.J., Huerta-Ocampo, I., Deisseroth, K., Capogna, M., and Bolam, J.P. (2011). Differential modulation of excitatory and inhibitory striatal synaptic transmission by histamine. J Neurosci 31, 15340-15351.

Feldman, D.E. (2012). The spike-timing dependence of plasticity. Neuron 75, 556-571.

Fisher, S.D., Robertson, P.B., Black, M.J., Redgrave, P., Sagar, M.A., Abraham, W.C., and Reynolds, J.N.J. (2017). Reinforcement determines the timing dependence of corticostriatal synaptic plasticity in vivo. Nat Commun 8, 334.

Fornal, C.A., Metzler, C.W., Marrosu, F., Ribiero-do-Valle, L.E., and Jacobs, B.L. (1996). A subgroup of dorsal raphe serotonergic neurons in the cat is strongly activated during oral-buccal movements. Brain Res 716, 123-133.

Giacomini, C., Mahajani, S., Ruffilli, R., Marotta, R., and Gasparini, L. (2016). Lamin B1 protein is required for dendrite development in primary mouse cortical neurons. Mol Biol Cell 27, 35-47.

Gilles, J.F., Dos Santos, M., Boudier, T., Bolte, S., and Heck, N. (2017). DiAna, an ImageJ tool for object-based 3D co-localization and distance analysis. Methods 115, 55-64.

Giorgi, A., Migliarini, S., Galbusera, A., Maddaloni, G., Mereu, M., Margiani, G., Gritti, M., Landi, S., Trovato, F., Bertozzi, S.M., *et al*. (2017). Brain-wide Mapping of Endogenous Serotonergic Transmission via Chemogenetic fMRI. Cell Rep 21, 910-918.

Goddard, A.W., Shekhar, A., Whiteman, A.F., and McDougle, C.J. (2008). Serotoninergic mechanisms in the treatment of obsessive-compulsive disorder. Drug Discov Today 13, 325-332.

Golding, N.L., Jung, H.Y., Mickus, T., and Spruston, N. (1999). Dendritic calcium spike initiation and repolarization are controlled by distinct potassium channel subtypes in CA1 pyramidal neurons. J Neurosci 19, 8789-8798.

Golding, N.L., Staff, N.P., and Spruston, N. (2002). Dendritic spikes as a mechanism for cooperative long-term potentiation. Nature 418, 326-331.

Grueter, B.A., Brasnjo, G., and Malenka, R.C. (2010). Postsynaptic TRPV1 triggers cell type-specific long-term depression in the nucleus accumbens. Nature neuroscience 13, 1519-1525.

Hannon, J., and Hoyer, D. (2008). Molecular biology of 5-HT receptors. Behav Brain Res 195, 198-213.

Hebert-Chatelain, E., Reguero, L., Puente, N., Lutz, B., Chaouloff, F., Rossignol, R., Piazza, P.V., Benard, G., Grandes, P., and Marsicano, G. (2014). Cannabinoid control of brain bioenergetics: Exploring the subcellular localization of the CB1 receptor. Mol Metab 3, 495-504.

Heck, N., Dos Santos, M., Amairi, B., Salery, M., Besnard, A., Herzog, E., Boudier, T., Vanhoutte, P., and Caboche, J. (2015). A new automated 3D detection of synaptic contacts reveals the formation of cortico-striatal synapses upon cocaine treatment in vivo. Brain Struct Funct 220, 2953-2966.

Herzog, E., Landry, M., Buhler, E., Bouali-Benazzouz, R., Legay, C., Henderson, C.E., Nagy, F., Dreyfus, P., Giros, B., and El Mestikawy, S. (2004). Expression of vesicular glutamate transporters, VGLUT1 and VGLUT2, in cholinergic spinal motoneurons. Eur J Neurosci 20, 1752-1760.

Herzog, E., Nadrigny, F., Silm, K., Biesemann, C., Helling, I., Bersot, T., Steffens, H., Schwartzmann, R., Nagerl, U.V., El Mestikawy, S., *et al*. (2011). In vivo imaging of intersynaptic vesicle exchange using VGLUT1 Venus knock-in mice. J Neurosci 31, 15544-15559.

Higley, M.J., and Sabatini, B.L. (2010). Competitive regulation of synaptic Ca2+ influx by D2 dopamine and A2A adenosine receptors. Nature neuroscience 13, 958-966.

Hikida, T., Kimura, K., Wada, N., Funabiki, K., and Nakanishi, S. (2010). Distinct roles of synaptic transmission in direct and indirect striatal pathways to reward and aversive behavior. Neuron 66, 896-907.

Huerta-Ocampo, I., Mena-Segovia, J., and Bolam, J.P. (2014). Convergence of cortical and thalamic input to direct and indirect pathway medium spiny neurons in the striatum. Brain Struct Funct 219, 1787-1800.

Jacobs, B.L., and Fornal, C.A. (1999). Activity of serotonergic neurons in behaving animals. Neuropsychopharmacology 21, 9S-15S.

Johnson, K.A., Mateo, Y., and Lovinger, D.M. (2017). Metabotropic glutamate receptor 2 inhibits thalamically-driven glutamate and dopamine release in the dorsal striatum. Neuropharmacology 117, 114-123.

Kilkenny, C., Browne, W.J., Cuthill, I.C., Emerson, M., and Altman, D.G. (2010). Improving bioscience research reporting: The ARRIVE guidelines for reporting animal research. J Pharmacol Pharmacother 1, 94-99.

King, M.V., Marsden, C.A., and Fone, K.C. (2008). A role for the 5-HT(1A), 5-HT4 and 5-HT6 receptors in learning and memory. Trends Pharmacol Sci 29, 482-492.

Kravitz, A.V., Freeze, B.S., Parker, P.R., Kay, K., Thwin, M.T., Deisseroth, K., and Kreitzer, A.C. (2010). Regulation of parkinsonian motor behaviours by optogenetic control of basal ganglia circuitry. Nature 466, 622-626.

Kravitz, A.V., Tye, L.D., and Kreitzer, A.C. (2012). Distinct roles for direct and indirect pathway striatal neurons in reinforcement. Nature neuroscience 15, 816-818.

Kreitzer, A.C., and Malenka, R.C. (2007). Endocannabinoid-mediated rescue of striatal LTD and motor deficits in Parkinson's disease models. Nature 445, 643-647.

Lee, S.J., Escobedo-Lozoya, Y., Szatmari, E.M., and Yasuda, R. (2009). Activation of CaMKII in single dendritic spines during long-term potentiation. Nature 458, 299-304.

Liu, G., and Voyno-Yasenetskaya, T.A. (2005). Radixin stimulates Rac1 and Ca2+/calmodulin-dependent kinase, CaMKII: cross-talk with Galpha13 signaling. J Biol Chem 280, 39042-39049.

Luscher, C., Nicoll, R.A., Malenka, R.C., and Muller, D. (2000). Synaptic plasticity and dynamic modulation of the postsynaptic membrane. Nature neuroscience 3, 545-550.

Mathur, B.N., Capik, N.A., Alvarez, V.A., and Lovinger, D.M. (2011). Serotonin induces long-term depression at corticostriatal synapses. J Neurosci 31, 7402-7411.

Mathur, B.N., and Lovinger, D.M. (2012). Serotonergic action on dorsal striatal function. Parkinsonism Relat Disord 18 Suppl 1, S129-131.

Matias, S., Lottem, E., Dugue, G.P., and Mainen, Z.F. (2017). Activity patterns of serotonin neurons underlying cognitive flexibility. eLife 6.

Mereu, M., Contarini, G., Buonaguro, E.F., Latte, G., Manago, F., Iasevoli, F., de Bartolomeis, A., and Papaleo, F. (2017). Dopamine transporter (DAT) genetic hypofunction in mice produces alterations consistent with ADHD but not schizophrenia or bipolar disorder. Neuropharmacology 121, 179-194.

Mereu, M., Tronci, V., Chun, L.E., Thomas, A.M., Green, J.L., Katz, J.L., and Tanda, G. (2015). Cocaine-induced endocannabinoid release modulates behavioral and neurochemical sensitization in mice. Addiction biology 20, 91-103.

Migliarini, S., Pacini, G., Pelosi, B., Lunardi, G., and Pasqualetti, M. (2013). Lack of brain serotonin affects postnatal development and serotonergic neuronal circuitry formation. Mol Psychiatry 18, 1106-1118.

Morishita, W., Marie, H., and Malenka, R.C. (2005). Distinct triggering and expression mechanisms underlie LTD of AMPA and NMDA synaptic responses. Nature neuroscience 8, 1043-1050.

Navailles, S., and De Deurwaerdere, P. (2011). Presynaptic control of serotonin on striatal dopamine function. Psychopharmacology (Berl) 213, 213-242.

Nazzaro, C., Greco, B., Cerovic, M., Baxter, P., Rubino, T., Trusel, M., Parolaro, D., Tkatch, T., Benfenati, F., Pedarzani, P., and Tonini, R. (2012). SK channel modulation rescues striatal plasticity and control over habit in cannabinoid tolerance. Nature neuroscience.

Nelson, A.B., Gittis, A.H., and du Lac, S. (2005). Decreases in CaMKII activity trigger persistent potentiation of intrinsic excitability in spontaneously firing vestibular nucleus neurons. Neuron 46, 623-631.

O'Hare, J.K., Ade, K.K., Sukharnikova, T., Van Hooser, S.D., Palmeri, M.L., Yin, H.H., and Calakos, N. (2016). Pathway-Specific Striatal Substrates for Habitual Behavior. Neuron 89, 472-479.

Parker, P.R., Lalive, A.L., and Kreitzer, A.C. (2016). Pathway-Specific Remodeling of Thalamostriatal Synapses in Parkinsonian Mice. Neuron 89, 734-740.

Pelosi, B., Migliarini, S., Pacini, G., Pratelli, M., and Pasqualetti, M. (2014). Generation of Pet1210-Cre transgenic mouse line reveals non-serotonergic expression domains of Pet1 both in CNS and periphery. PLoS One 9, e104318.

Plotkin, J.L., Day, M., Peterson, J.D., Xie, Z., Kress, G.J., Rafalovich, I., Kondapalli, J., Gertler, T.S., Flajolet, M., Greengard, P., *et al*. (2014). Impaired TrkB receptor signaling underlies corticostriatal dysfunction in Huntington's disease. Neuron 83, 178-188.

Plotkin, J.L., Shen, W., Rafalovich, I., Sebel, L.E., Day, M., Chan, C.S., and Surmeier, D.J. (2013). Regulation of dendritic calcium release in striatal spiny projection neurons. J Neurophysiol 110, 2325-2336.

Ponimaskin, E.G., Profirovic, J., Vaiskunaite, R., Richter, D.W., and Voyno-Yasenetskaya, T.A. (2002). 5-Hydroxytryptamine 4(a) receptor is coupled to the Galpha subunit of heterotrimeric G13 protein. J Biol Chem 277, 20812-20819.

Popescu, A.T., Saghyan, A.A., and Pare, D. (2007). NMDA-dependent facilitation of corticostriatal plasticity by the amygdala. Proc Natl Acad Sci U S A 104, 341-346.

Shen, W., Flajolet, M., Greengard, P., and Surmeier, D.J. (2008). Dichotomous dopaminergic control of striatal synaptic plasticity. Science 321, 848-851.

Shen, W., Plotkin, J.L., Francardo, V., Ko, W.K., Xie, Z., Li, Q., Fieblinger, T., Wess, J., Neubig, R.R., Lindsley, C.W., *et al*. (2015). M4 Muscarinic Receptor Signaling Ameliorates Striatal Plasticity Deficits in Models of L-DOPA-Induced Dyskinesia. Neuron 88, 762-773.

Shindou, T., Ochi-Shindou, M., and Wickens, J.R. (2011). A Ca(2+) threshold for induction of spike-timing-dependent depression in the mouse striatum. J Neurosci 31, 13015-13022.

Shuen, J.A., Chen, M., Gloss, B., and Calakos, N. (2008). Drd1a-tdTomato BAC transgenic mice for simultaneous visualization of medium spiny neurons in the direct and indirect pathways of the basal ganglia. J Neurosci 28, 2681-2685.

Sippy, T., Lapray, D., Crochet, S., and Petersen, C.C. (2015). Cell-Type-Specific Sensorimotor Processing in Striatal Projection Neurons during Goal-Directed Behavior. Neuron 88, 298-305.

Smith, M.R., Nelson, A.B., and Du Lac, S. (2002). Regulation of firing response gain by calcium-dependent mechanisms in vestibular nucleus neurons. J Neurophysiol 87, 2031-2042.

Smith, Y., Galvan, A., Ellender, T.J., Doig, N., Villalba, R.M., Huerta-Ocampo, I., Wichmann, T., and Bolam, J.P. (2014). The thalamostriatal system in normal and diseased states. Frontiers in systems neuroscience 8, 5.

Sudhof, T.C. (2012). The presynaptic active zone. Neuron 75, 11-25.

Tang, S., and Yasuda, R. (2017). Imaging ERK and PKA Activation in Single Dendritic Spines during Structural Plasticity. Neuron 93, 1315-1324 e1313.

Tecuapetla, F., Jin, X., Lima, S.Q., and Costa, R.M. (2016). Complementary Contributions of Striatal Projection Pathways to Action Initiation and Execution. Cell 166, 703-715.

Thorn, C.A., and Graybiel, A.M. (2010). Pausing to regroup: thalamic gating of cortico-basal ganglia networks. Neuron 67, 175-178.

Threlfell, S., Lalic, T., Platt, N.J., Jennings, K.A., Deisseroth, K., and Cragg, S.J. (2012). Striatal dopamine release is triggered by synchronized activity in cholinergic interneurons. Neuron 75, 58-64.

Tritsch, N.X., Ding, J.B., and Sabatini, B.L. (2012). Dopaminergic neurons inhibit striatal output through non-canonical release of GABA. Nature 490, 262-266.

Trusel, M., Cavaccini, A., Gritti, M., Greco, B., Saintot, P.P., Nazzaro, C., Cerovic, M., Morella, I., Brambilla, R., and Tonini, R. (2015). Coordinated Regulation of Synaptic Plasticity at Striatopallidal and Striatonigral Neurons Orchestrates Motor Control. Cell Rep 13, 1353-1365.

van Welie, I., and du Lac, S. (2011). Bidirectional control of BK channel open probability by CAMKII and PKC in medial vestibular nucleus neurons. J Neurophysiol 105, 1651-1659.

Vicente, A.M., Galvao-Ferreira, P., Tecuapetla, F., and Costa, R.M. (2016). Direct and indirect dorsolateral striatum pathways reinforce different action strategies. Curr Biol 26, R267-269.

Wu, Y.W., Kim, J.I., Tawfik, V.L., Lalchandani, R.R., Scherrer, G., and Ding, J.B. (2015). Input- and Cell-Type-Specific Endocannabinoid-Dependent LTD in the Striatum. Cell Rep 10, 75-87.

Yagishita, S., Hayashi-Takagi, A., Ellis-Davies, G.C., Urakubo, H., Ishii, S., and Kasai, H. (2014). A critical time window for dopamine actions on the structural plasticity of dendritic spines. Science 345, 1616-1620.

Zhai, S., Tanimura, A., Graves, S.M., Shen, W., and Surmeier, D.J. (2017). Striatal synapses, circuits, and Parkinson's disease. Curr Opin Neurobiol 48, 9-16.

Zhou, Y.D., Acker, C.D., Netoff, T.I., Sen, K., and White, J.A. (2005). Increasing Ca2+ transients by broadening postsynaptic action potentials enhances timing-dependent synaptic depression. Proc Natl Acad Sci U S A 102, 19121-19125.

Figure Legends

Figure 1. Chemogenetic inhibition of 5-HT release in the DLS promotes the induction of t-LTD at dSPN glutamatergic synapses

(**A**) (Top) Experimental configuration in horizontal brain slices containing the dorsolateral striatum (DLS). Schematic shows glutamatergic cortical and thalamic inputs to dSPNs, as well as dopaminergic and serotonergic afferents, which are recruited following intrastriatal electrical stimulation. (Bottom) Confocal laser scanning microscopy images of triple immunofluorescence for adenosine A2A receptor (A2AR), substance P (SP) and biotin in patch-recorded neurons.

(**B**) (Top) The post-pre pairing protocol for the induction of t-LTD. (Bottom) In dSPNs from naïve mice, t-LTD was not induced by the post-pre timing pairing (dSPN, n = 8, 7 mice; RM1WA $F_{7,44}$ = 1, p = 0.4).

(**C**) Experimental configuration in brain slices from hM4Di$^{+/-}$/Pet1$_{210}$-Cre mice, highlighting the 5-HT terminals (green) originating from the dorsal raphe nucleus (DRN). In DLS dSPNs from these mice, bath perfusion of CNO (5 μM; blue bar) during STDP gated a form of t-LTD, which was absent under control conditions (dSPN$_{DREADD}$ + CNO, n = 8, 7 mice; RM1WA $F_{7,44}$ = 8, p < 0.0001, p < 0.05 Tukey; dSPN$_{DREADD}$, n = 5, 5 mice; RM1WA $F_{4,44}$ = 1.5, p = 0.3; dSPN$_{DREADD}$ + CNO versus dSPN$_{DREADD}$, *p < 0.05, Mann-Whitney test).

(**B**, **C**) In this figure, and in the analogous plots that follow throughout the manuscript, data are presented as a time-course (mean ± s.e.m.) of normalized EPSP amplitudes and normalized Rinp. Scatterplot summarizes the ratios of synaptic responses after (a) and before (b) the STDP, at the time points indicated. Insets represent superimposed averaged recordings (ten traces) before and after the delivery of the STDP protocol (vertical bar) (See also **Figures S1-S4**).

Figure 2. Antagonizing the 5-HT4R subtype is a permissive condition for t-LTD to occur

(**A**) t-LTD was observed at glutamatergic dSPN synapses when the post-pre STDP protocol was delivered in the presence of the 5-HT4R antagonists GR113808 or RS39604 (5 μM; GR113808, n =

8, 7 mice; RM1WA $F_{7,44} = 7$, $p = 0.003$, $p < 0.05$ Tukey; RS39604, n = 10, 9 mice; RM1WA $F_{9,44} = 14$, $p < 0.0001$, $p < 0.05$ Tukey; 1WA $F_{2,23} = 10$, $p = 0.0008$, dSPN+ GR113808 versus dSPN, *p< 0.05, dSPN+ RS39604 versus dSPN, ***p < 0.001; Tukey). The two 5-HT4R antagonists were applied throughout the entire duration of the recording. Solid black line (average) is the time-course from **Figure 1B**, reported here for reference.

(**B**) t-LTD gated by RS39604 was not blocked by the CB1R antagonist AM251 (4 μM; dSPN + RS39604/AM251, n = 5, 4 mice; RM1WA $F_{4,44} = 10$ $p = 0.001$, $p < 0.05$ Tukey; dSPN + AM251/RS39604 versus dSPN + RS39604, $p = 0.6$, Mann-Whitney test). Solid green line (average) is t-LTD from (**A**) obtained in the presence of RS39604, reported here for reference.

(**C**) t-LTD induced with the post-pre pairing upon application of RS39604 (5 μM) was not associated with changes in paired-pulse-ratio (PPR). (Left) Plot shows the normalized first peak (p1) and second peak (p2) amplitudes of synaptic responses generated by twin stimuli at a 50-ms interval as a function of time (dSPN + RS39604, n = 6, 5 mice; p1, RM1WA $F_{5,44} = 5$ $p< 0.0001$, $p < 0.05$ Tukey; p2, RM1WA $F_{5,44} = 6$ $p < 0.0001$, $p < 0.05$ Tukey). (Right) Box-plot diagram indicates the PPRs of baseline (black box), and after STDP (red box) at the time points indicated ($p = 0.5$, paired t-test). The values are the minimum, median (bar inside the box), and the maximum. PPR is expressed as the ratio between the amplitude of the second and first EPSPs.

(**D**) In the presence of RS39604, t-LTD was blocked by intracellular application of the endocytosis-disrupting peptides D15 (1.5 mM; dSPN + D15, n = 8, 8 mice; RM1WA $F_{7,44} = 1.7$ $p = 0.17$) or $GluA2_{3Y}$ (100 μg/ml; dSPN + $GluA2_{3Y}$, n = 6, 5 mice; RM1WA $F_{5,44} = 1$ $p = 0.4$). The specificity of action of D15 and $GluA2_{3Y}$ was confirmed by their respective control peptides (S15 for D15; $GluA2_{3A}$ for $GluA2_{3Y}$) (S15, 1.5 mM; dSPN + S15, n = 5, 3 mice; RM1WA $F_{4,44} = 4$, $p = 0.03$, $p< 0.05$ Tukey; $GluA2_{3A}$, 100 μg/ml; dSPN + $GluA2_{3A}$, n = 6, 5 mice; RM1WA $F_{5,44} = 8$, $p = 0.0007$, $p < 0.05$ Tukey; 1WA, $F_{4,28} = 7$, $p= 0.0004$; dSPN + S15 versus dSPN, **p < 0.01 ; dSPN + D15 versus dSPN, $p = 0.9$, dSPN + D15 versus dSPN + S15, *p < 0.05; dSPN + $GluA2_{3A}$ versus dSPN, *p < 0.05; dSPN +

$GluA2_{3Y}$ versus dSPN, p = 1; dSPN + $GluA2_{3Y}$ versus dSPN + $GluA2_{3A}$, *p < 0.05; Tukey). Solid black line (average) is the time-course from **Figure 1B**, reported here for reference.

(**A-D**) (Insets, left) In this figure, and throughout the manuscript, schematics depict proposed signaling pathway targeted by the defined drug, unless specified otherwise (See also **Figure S4**).

Figure 3. 5-HT signaling modulates bAP-induced dendritic Ca^{2+} transients in dSPNs

(**A**) (Top left) Maximum-intensity projection images of a dSPN filled with Alexa 568. Blue dotted circle lines delimit the region of proximal dendrites, 30-50 μm from the soma. (Bottom left) High-magnification of a dSPN proximal dendrite from which line scans were taken (yellow dotted line). (Center) Dendritic Ca^{2+} transients and the corresponding relative changes in fluorescence that are induced by one bout of the post-pre STDP paradigm (1b-STDP, inset) for control conditions, and after 10 to 15 min (n = 8, 4 mice; paired t-test, p = 0.4). (**B**) Chemogenetic inhibition of 5-HT release in the DLS of $hM4Di^{+/-}/Pet1_{210}$-Cre mice enhanced dendritic Ca^{2+} transients in response to 1b-STDP (n = 11, 6 mice).

(**B-G**) (Left) Comparison of Ca^{2+} transients in response to 1b-STDP (**B-D**) or to a burst pattern of bAPs (**E-G**), before and after a specific pharmacological manipulation, as indicated.

(**A-G**) (Right) Plot summary of modulation of dendritic Ca^{2+} measured as area under the curve (AUC) of the fluorescence transients, in control conditions and with pharmacological manipulations, as indicated [**A**, **B**, **C** (GR113808, n = 15, 10 mice; RS39604, n = 14, 11 mice), **E** (n = 10, 4 mice), **G** (n = 10, 4 mice), **p < 0.01, paired t-test; **D**, n = 9, 5 mice; RM1WA, $F_{8,2}$ = 20 p < 0.0001, paxilline versus control, ***p < 0.001; paxilline + RS39604 versus control, ***p < 0.001; paxilline versus paxilline + RS39604, p = 1; Tukey; **F**, n = 7, 6 mice; RM1WA, $F_{6,2}$=9 p = 0.005, paxilline versus control, **p< 0.01; paxilline + RS67333 versus control, *p = 0.01, Tukey; paxilline versus paxilline + RS67333, p = 1; Tukey]. (See also **Figure S5**).

Figure 4. Decreased 5-HT signaling gates t-LTD at thalamo-dSPN synapses

(**A**) Confocal images of horizontal sections of Thy1-ChR2 transgenic mice; scale bar, 500 μm; Ctx, cortex; Str, striatum; Hip, hippocampus; Thal, thalamus. Inset shows ChR2-eYFP expressing axon terminals in the DLS; scale bar, 10 μm.

(**B**) Schematic of recording configuration in dSPNs. (Top) Corticostriatal stimulation evoked by 470 nm LED pulses through the microscope objective was performed before and after the STDP protocol. (Bottom) During the post-pre STDP paradigm, light stimulation of cortical terminals was replaced by local electrical stimulation. (**C**) The post-pre STDP protocol failed to induce plasticity of o-EPSP$_{Ctx}$ either under control conditions (dSPN$_{Ctx}$, n = 7, 6 mice; RM1WA $F_{6,44}$ =1.1, p = 0.4) or upon RS39604 application (dSPN$_{Ctx}$ + RS39604, n = 8, 8 mice; RM1WA $F_{7,44}$ = 0.8, p = 0.5).

(**D**) (Left and Top Right) rAAV5-CaMKIIa-ChR2(H134R)-eYFP expression targeting the thalamus (Thal); scale bar, 500 μm; Ctx, cortex; Str, striatum; Hip, hippocampus. (Inset) ChR2-eYFP^{+} axons in the DLS; scale bar, 10 μm. (Right) Schematic of recording configuration of o-EPSP$_{Thal}$ evoked by 470 nm LED pulses (Center Right), and during the delivery of the STDP paradigm (Bottom Right).

(**E**) t-LTD is induced at thalamo-dSPN synapses upon 5-HT4R inhibition (dSPN$_{Thal,}$ n = 6, 6 mice; RM1WA $F_{5,44}$ = 1.5, p = 0.3; dSPN$_{Thal}$ + RS39604, n = 8, 4 mice; RM1WA $F_{7,44}$ =10, p = 0.0002, p< 0.05 Tukey; dSPN$_{Thal}$ + RS39604 versus dSPN$_{Thal}$, **p< 0.01, Mann-Whitney test).

(**F**) In hM4Di$^{+/-}$/Pet1$_{210}$-Cre mice injected with the rAAV5-CaMKIIa-ChR2(H134R)-eYFP virus in the thalamus, bath application of CNO (5 μM) gated t-LTD of o-EPSP$_{thal}$ in response to STDP (dSPN$_{DREADD_Thal}$, n = 7, 4 mice; RM1WA $F_{6,44}$ =1.8, p = 0.1; dSPN$_{DREADD_Thal}$ + CNO, n = 7, 4 mice; RM1WA $F_{6,44}$ = 10, p = 0.0002, p <0.05 Tukey; dSPN$_{DREADD_Thal}$ + CNO versus dSPN$_{DREADD_Thal}$, ***p < 0.001, Mann-Whitney test). (See also **Figure S6**-**S8**).

Figure 5. Activation of 5-HT signaling blunts t-LTD induction at thalamo-dSPN synapses

(**A**) (Left) Schematic of recording configuration of o-EPSP$_{Thal}$ evoked by 470 nm LED pulses, and during the delivery of the optogenetic STDP paradigm. (Right) The o-STDP protocol induced t-LTD

at thalamostriatal synapses (n = 6, 2 mice; RM1WA $F_{5,44} = 4$, $p < 0.0001$, $p < 0.05$ Tukey); plasticity was blocked by application of the 5-HT4R agonist RS67333 (n = 8, 3 mice; RM1WA $F_{7,44} = 2$, $p = 0.13$; $dSPN_{Thal}$ + RS67333 versus $dSPN_{Thal}$, *$p < 0.05$, Mann-Whitney test).

(**B**) (Left) Schematic of bilateral virus injection [rAAV5-EF1a-DIO-hChR2(H134R)-eYFP] in the DRN of $Petl_{210}$-Cre mice. (**1**-**3**) Confocal images show the expression of 5-HT (red), YFP (green) and merge in the DRN. DAPI nuclear staining (inset in **2**) identifies the two injection sites. Scale bar 200 μm. (**4**-**9**) High-resolution confocal images showing SERT (red) and YFP (green) expression, and their co-localization (merge) in serotonergic afferents to the DLS. Scale bars 20 μm (**4**-**6**) and 10 μm (**7**-**9**).

(**C**) (Top) Experimental configuration in para-horizontal slices, showing the DLS, lateral globus pallidus (LGP), thalamic reticular nucleus (Rt), and the DRN. (Bottom) The electric post-pre pairing protocol (Thal-STDP) for the induction of t-LTD and timing of $5\text{-}HT_{opto}$ application.

(**D**) (Left) Recording configuration. (Right) In dSPNs, t-LTD of $e\text{-}EPSP_{Thal}$ ($dSPN_{e\text{-}Thal}$, n = 6, 6 mice; RM1WA $F_{5,44} = 4$, $p < 0.0001$, $p < 0.05$ Tukey) was suppressed by light-induced 5-HT release ($dSPN_{e\text{-}Thal}$ + $5\text{-}HT_{opto}$, n = 8, 6 mice; RM1WA $F_{7,44} = 0.8$, $p = 0.9$), and rescued by application of the 5-HT4R antagonist RS39604 (5 μM, $dSPN_{e\text{-}Thal}$ + $5\text{-}HT_{opto}$ + RS39604, n = 5, 4 mice; RM1WA $F_{4,44} = 18$, $p = 0.0003$, $p < 0.05$ Tukey; 1WA, $F_{2,16} = 16$, $p = 0.0002$; $dSPN_{e\text{-}Thal}$ versus $dSPN_{e\text{-}Thal}$ + $5\text{-}HT_{opto}$, **$p < 0.01$; $dSPN_{e\text{-}Thal}$ versus $dSPN_{e\text{-}Thal}$ + $5\text{-}HT_{opto}$ + RS39604, $p = 0.2$; $dSPN_{e\text{-}Thal}$ + $5\text{-}HT_{opto}$ versus $dSPN_{e\text{-}Thal}$ + $5\text{-}HT_{opto}$ + RS39604, ***$p < 0.001$; Tukey).

Figure 6. Postsynaptic subcellular localization of 5-HT4R

(**A**) (Left) 3D volume rendering of confocal image stack showing 5-HT4R and glutamatergic boutons in the DLS. Cortical VGLUT1 positive boutons were imaged in VGLUT1-Venus knock-in mice. Thalamic VGLUT2 boutons were imaged in VGLUT2-Cre mice injected in the thalamus with the AAV-FLEX-eGFP virus. Co-localization with immunostained presynaptic active zone protein

Bassoon allowed the selection of thalamic boutons from the segmented images (see **Figure S9**). (Right) Measurements of 3D border-to-border minimal distance from VGLUT1-positive boutons and VGLUT2-positive boutons to the closest 5-HT4R. 18 to 24 image stacks from 2 sections from 3 mice were analyzed. Each image stack corresponded to a field of view of 60 x 60 μm and 5 μm depth, and contained on average 4149 ± 118 VGLUT1-positive boutons and 658 ± 69 VGLUT2-positive boutons. The distance from VGLUT2 boutons to 5-HT4R was shorter than the distance between VGLUT1 boutons and 5-HT4R (****$p < 0.0001$, t-test). (**B**) 3D volume rendering of a dSPN dendrite labeled after injection in the DLS of a mix of AAV9-PPTA-CRE and AAV9-FLEX-tdTOMATO viruses with immunostained 5-HT4R. The dendritic shaft was reconstructed in 3D by using Neuronstudio software, the dendrite model then imported into ImageJ and the headspines were segmented. Eight dendritic segments, from 3 mice, for a total of 423 μm dendrite length with more than 1000 spines were analyzed. (Bottom left) 3D volume rendering of extracted dendritic shaft (red) and segmented spine head (a specific color is attributed to each spine head) with co-localizing 5-HT4R (white). Arrowheads indicate examples of 5-HT4R in shaft; arrows indicate 5-HT4R on spines. (Right) Percentage of 5-HT4R co-localizing with either dendritic shaft or spine head. (**C**) 3D volume rendering showing 5-HT4R (white) found in the contact between boutons from thalamic axons (green) and dendrite shaft (Top) or spine head (Bottom) from dSPNs (red). Only 5-HT4Rs co-localizing with thalamic axonal bouton and dendrite shaft or spine are shown. Thalamic axons were labeled by injecting AAV-FLEX-eGFP in the thalamus of VGLUT2-Cre mice. dSPNs were labeled by injecting AAV-PPTA-Cre and AAV-FLEX-tdTOMATO in the DLS. 5-HT4R was detected by immunolabeling. (See also **Figure S9**).

Figure 7. Proposed model for 5-HT-mediated regulation of postsynaptic dendritic Ca^{2+} signals during timing-dependent plasticity

(A) Stimulation of 5-HT4R during the post-pre STDP paradigm promotes phosphorylation of CaMKII at Thr286, thus boosting CaMKII activation, which in turn increases the function of BK

channels during bursts of bAPs, ultimately reducing dendritic bAP-induced Ca^{2+} influx. This reduction would tip the balance in favor of t-LTD suppression.

(B) From the opposite view, in the presence of neuromodulatory afferent stimulation, it is sufficient to inhibit 5-HT release, or to prevent the activation of the 5-HT4R subtype, to limit the activity of BK channels during the post-pre pairing, thus enhancing Ca^{2+} influx. This would promote the induction of t-LTD, which involves internalization of AMPAR.

STAR METHODS

CONTACT FOR REAGENTS AND RESOURCE SHARING

Further information and requests for resources and reagents should be directed to and will be fulfilled by the Lead Contact, Dr. Raffaella Tonini (raffaella.tonini@iit.it).

Distribution of the *Drd1a*-td Tomato BAC transgenic mouse line 5 is rescricted by MTA.

EXPERIMENTAL MODEL AND SUBJECT DETAILS

Animals

All procedures involving animals were carried out in accordance with the Italian Ministry of Health's directives (D.lgs 26/2014) regulating animal research. Animal experiments were designed in accordance with the ARRIVE (Animal Research: Reporting of In Vivo Experiments) guidelines (Kilkenny et al., 2010), with a commitment to refinement, reduction, and replacement, minimizing the number of mice. Drug, and test naïve male mice at postnatal day 35-80 were housed 4-5 per cage in a temperature- and humidity-controlled room under a 12:12 h light/dark cycle with lights on at 07:00, and fed regular laboratory chow with *ad libitum* access to water. The following mouse strains were used in this study: C57BL/6J (Charles River Laboratories; RRID: IMSR_JAX:000664), hM4Di$^{+/-}$/Pet1$_{210}$-Cre, hM4Di$^{+/-}$/Pet1$_{210}$-Cre^{0}, Pet1$_{210}$-Cre, hM4Di$^{+/-}$/Pet1$_{210}$-Cre/Tph2$^{GFP+/-}$ (Laboratory of Prof. Massimo Pasqualetti); B6.Cg-Tg(Thy1-COP4/EYFP)18Gfng/J (The Jackson Laboratory; RRID: IMSR_JAX:007612), Slc17a6$^{tm2(cre)Lowl}$/J (VGLUT2-Cre) (The Jackson Laboratory; RRID: IMSR_JAX:016963); Drd1a-td Tomato BAC transgenic mouse line 5 (Laboratory of Dr. N.Calakos) backcrossed to C57BL/6J; VGLUT1^{Venus} knock-in (Laboratory of Dr. Etienne Herzog and Laboratory of Dr. J. Caboche). For all strains, male mice were routinely bred with C57BL/6J females, with the exception of VGLUT2-Cre and VGLUT1^{Venus}, which were maintained in homozygosis. For production of hM4Di$^{+/-}$/Pet1$_{210}$-Cre animals, hM4Di$^{+/-}$ adult males were mated to Pet1$_{210}$-Cre transgenic females; progeny was genotyped for the presence of both

hM4Di in the ROSA26 locus and Cre. For production of hM4Di$^{+/-}$/Pet1$_{210}$-Cre/Tph2$^{GFP+/-}$ mice, hM4Di$^{+/-}$/Pet1$_{210}$-Cre males were mated to Tph2$^{GFP+/-}$ females. Progeny was genotyped for the presence of hM4Di in the ROSA26 locus, Cre, and GFP within the Tph2 locus.

METHOD DETAILS

Generation of the hM4Di knock-in mouse line

We generated the hM4Di^{DIO} conditional knock-in mouse line taking advantage of a gene targeting strategy allowing the insertion of the construct via homologous recombination within the *ROSA26* genomic locus. The in-frame fusion protein resulting from the hM4Di DREADD receptor and the mCherry reporter coding sequences was flanked by two couples of Lox sites (LoxP/Lox2722). The resulting cassette was isolated from the pAAV-hSyn-DIO-*hM4Di*/*mCherry* vector and cloned in the 3'-5' orientation within the pCX-CAG-*eGFP* plasmid downstream of the CAG promoter by replacing the *eGFP* sequence. Subsequently, the CAG-*hM4Di*/*mCherry* fragment was isolated from pCX-CAG-*hM4Di*/*mCherry* via SpeI/XbaI double digestion and cloned in the XbaI site of the pROSA26-1^{Sor} plasmid that had been previously modified by the addition of a *PvuI* recognition site downstream to the *pgk-DTa* cassette in place of the unique XhoI site. Finally, the SpeI/NheI fragment containing the *pgk-Neo*/*Kana* cassette was obtained from the pPSVKeoFRT plasmid and cloned into the unique XbaI site of the pROSA26-1^{Sor}-CAG-*hM4Di*/*mCherry* vector. PvuI-linearized targeting vector was electroporated into E14Tg2a.4 ES cells and G418 selection was maintained for 7 days as described (Giorgi et al., 2017). Among 192 G418-resistant ES cell colonies screened, 32 were positive recombinant clones as assessed by Southern blot analysis. Following karyotype analysis, recombinant ES cells were microinjected into C57BL/6 host blastocysts that were later reimplanted into pseudopregnant CD1 females. Germline transmission was achieved for the 60% of the 29 chimeras obtained. hM4DiDIO mice were born at normal Mendelian ratios and lived a normal lifespan with no obvious defects.

Animals were genotyped using DNA primers as follows: wild-type *ROSA26* allele forward 5'-GAGGGGAGTGTTGCAATACC-3' and reverse 5'-AGTCTAACTCGCGACACTGTA-3'. The $hM4Di^{DIO}$ knock-in allele was genotyped using the same forward primer as above in combination with the reverse primer 5'-GTCCCTATTGGCGTTACTATG-3'.

In vivo microdialysis

$hM4Di^{+/-}$/$Pet1_{210}$-Cre mice were anesthetized with Avertin (1.5 mg/kg) and placed in a stereotaxic frame (2B, 2biological Instruments) for probe implantation. Concentric dialysis probes were implanted either in the right or left dorsolateral striatum (DLS) (uncorrected coordinates from Paxinos & Franklin (2001): +0.38 AP, ± 2.0 ML, -3.8 DV). After surgery, mice were allowed to recover overnight in square Plexiglas cages (Allentown). Concentric dialysis probes were prepared using AN69 dialyzing membranes (Hospal Dasco, Bologna, Italy) as previously described (Mereu et al., 2017; Mereu et al., 2015). The exposed dialyzing surface of the membrane was limited to the lowest 2.00 mm portion of the probes, which were less than 18 mm in total length. Experiments were performed in freely moving animals in the same cage in which they recovered from surgery. Microdialysis test sessions started at 9 AM, approximately 22-24 hours after surgical procedures. Probes were connected to PE50 tubes and perfused with Ringer's solution (147.0 mM NaCl, 2.2mM $CaCl_2$ and 4.0 mM KCl) delivered through the dialysis probes by a 1.0 ml syringe, operated by a BAS BeeSyringe Pump Controller (BAS West Lafayette, IN, USA), at a constant flow rate of 1 µl/min. Collection of dialysate samples (20 µl) started after about 30 min, and extracellular serotonin levels were quantified using an HPLC apparatus equipped with a reverse-phase column (C83.5 µm, Waters, Milford, USA) and a coulometric electrochemical detector (ESA Coulochem II, Bedford, USA). At the end of each experiment, mice were sacrificed and their brains were removed and stored in formalin (4%) before histological analysis. Brains were cut in serial coronal slices (100 µm) to locate the placement of the microdialysis probe.

Viral injections for optogenetic experiments

Five- to six-week-old mice were anesthetized (2% isofluorane) and placed in a stereotaxic frame. To measure light-induced EPSPs at cortico- and thalamostriatal connections on dSPNs and iSPNs, C57BL/6J and hM4Di$^{+/-}$/Pet1$_{210}$-Cre mice were injected with rAAV5-CaMKIIa-ChR2(H134R)-eYFP virus (UNC Vector Core, Chapel Hill, North Carolina). The motor cortex M1 (+1.1 AP; ±1.6 ML; -0.8 DV from brain surface) or the thalamus was targeted (-2.3 AP; ± 0.75 ML; -3.5 DV). A volume of 0.5 µl/site of virus was injected at a rate of 0.1 µl/min. To measure the effect of the release of serotonin on electrically-induced EPSPs at thalamostriatal connections on dSPNs, Pet1$_{210}$-Cre mice were injected with rAAV5-EF1a-DIO-hChR2(H134R)-eYFP virus (UNC Vector Core, Chapel Hill, North Carolina). The dorsal raphe nucleus (DRN) was targeted (-4.36 AP; ±0.5 ML; -3, -4 DV). A volume of 0.8 µl/site of virus was injected at a rate of 0.1 µl/min. Mice were used for electrophysiological recordings 4-6 weeks after the injection.

Electrophysiology

Slice preparation

Mice were anesthetized with isofluorane and decapitated, and their brains were transferred to ice-cold dissecting artificial cerebrospinal fluid (aCSF) containing 110 mM choline chloride, 2.5 mM KCl, 1.25 mM NaH_2PO_4, 7 mM $MgSO_4$, 0.5 mM $CaCl_2$, 25 mM $NaHCO_3$, 25 mM D-glucose, 11.6 mM sodium-L-ascorbate and 3.1 mM sodium pyruvate, saturated with 95% O_2 and 5% CO_2. Coronal sections (250 µm thick), horizontal slices (270 µm thick) and para-horizontal slices (20° oblique) were cut using a Vibratome 1000S (Leica, Wetzlar, Germany), then transferred to aCSF containing 115 mM NaCl, 3.5 mM KCl, 1.2 mM NaH_2PO_4, 1.3 mM $MgCl_2$, 2 mM $CaCl_2$, 25 mM $NaHCO_3$ and 25 mM D-glucose and aerated with 95% O_2 and 5% CO_2. Following 20 min of incubation at 32°C, slices were kept at 22-24°C. During experiments, slices were continuously superfused with aCSF at a rate of 2 ml/min at 28°C.

Electrophysiological recordings

Whole-cell patch-clamp recordings were made on striatal projection neurons (SPNs) of the dorsolateral striatum (DLS) in horizontal or para-horizontal slices (20° oblique cut), or in neurons of the dorsal raphe nucleus (DRN) in coronal slices. Intracellular solution contained 130 mM $KMeSO_4$, 5 mM KCl, 5 mM NaCl, 10 mM HEPES, 0.1 mM EGTA, 2 mM $MgCl_2$, 0.05 mM $CaCl_2$, 2 mM Na_2-ATP and 0.4 mM Na_3-GTP (pH 7.2-7.3, 280-290 mOsm/kg).

In the DLS, excitatory postsynaptic potentials (EPSPs) were induced at 0.1 Hz in the presence of the $GABA_A$ receptor antagonist gabazine (10 μM) by intrastriatal electrical stimulation using a concentric bipolar electrode (40-100 μA; 40-80 μs; FHC, Bowdoin, Maine) or by optogenetic stimulation of cortical or thalamic afferents using short blue light pulses (range 0.1-1 ms at 470 nm) of LED light delivered through the microscope objective (CoolLED, pE-100, Andover, Hampshire, United Kingdom). STDP-LTD was induced using a protocol consisting of 20 bouts of EPSPs paired with bAPs, delivered 10 s apart. Each bout consisted of five bursts (120 ms apart), each composed of three bAPs at 50 Hz followed by one EPSP (negative timing). The onset of the EPSPs followed the peak of the last postsynaptic action potential in the burst by 10 ms ($\Delta t = 10$ ms). During plasticity induction, postsynaptic neurons were depolarized from −80 mV to −70 mV. Data were excluded when the input resistance (R_{inp}) changed >20%. In $Pet1_{210}$-Cre mice expressing ChR2 in the DRN, thalamic afferents were stimulated by placing the stimulation electrode in the thalamus close to the border with the thalamic reticular nucleus. To induce the release of serotonin from DRN afferents in the DLS, blue light pulses (10 ms duration at 470 nm) of LED light were delivered through the microscope objective (CoolLED, pE-100, Andover, Hampshire, United Kingdom) at the time of presynaptic stimulation evoked during the STDP protocol. BK-channel mediated current was recorded in voltage-clamp configuration in response to a depolarizing voltage ramp from -80 to 110 mV (rate 0.1 mV/ms). Data are reported without corrections for liquid junction potentials. Data were acquired using a Multiclamp 700B amplifier controlled by pClamp 10 software (Molecular Device), filtered at 2.5 kHz and sampled at 10 kHz (voltage clamp), or filtered at 10 kHz and sampled at 20 kHz (current-clamp) with

a (Digidata 1322, Molecular Device). For statistical purposes (RM2WA analysis; **Figure S5B**), data were filtered at 0.1 kHz.

Imaging

Ca^{2+} transients were imaged with 100 μM Fluo-4 (ThermoFisher Scientific , Carlsbad, California) dissolved in the intracellular recording solution. Alexa 568 (10 μM, ThermoFisher Scientific, Carlsbad, California) was used for visualization of cell bodies and dendrites. SPNs were filled with Alexa 568 and Fluo-4 via the patch electrode for 20 min before imaging to allow dye equilibration in the proximal dendrites. Whole-cell maximum-projection images of the soma and dendrites were acquired with 0.4 μm^2 pixels with 15 μs pixel dwell time; ~120 images were taken with 0.4 μm focal steps. Drugs were bath applied for 10 min.

Two-photon Ca^{2+} imaging was performed with a Leica SP5 AOBS upright DM6000 CFS microscope coupled with a 2P laser Chameleon Ultra Coherent and equipped with a Leica 25x NA 0.95 water immersion objective. The fluorescence emission was collected with an external non-descanned photomultiplier detector equipped with a 525/50 emission filter. Green fluorescence line-scan signals were acquired at 6 ms and 256 pixels per line, with 0.1 μm pixels and 20 μs pixel dwell time. The laser-scanned images were acquired with 800 nm light pulsed at 90 MHz (pulse duration: ~250 fs). The line scan was used to record the fluorescence elicited by one bout of the STDP protocol. Images were collected with LAS AF Leica software and analyzed using ImageJ software (version 1.45, http://rsb.info.nih.gov/ij/, NIH, Maryland) and Origin 9.1 (OriginLab Corporation, Northampton, Massachussets). For each recording, background fluorescence was determined from a cell-free area of comparable size to that of the line-scan image. After subtracting the averaged background signal, fluorescence values were recorded for 200 ms before the triggering the STDP protocol and averaged to give the basal fluorescence (F_{basal}). The amplitude of the fluorescence transients at the recording sites was expressed as the fractional change in basal fluorescence, $(F-F_{basal})/F_{basal,}$ ($\Delta F/F$), which is approximately proportional to the changes in intracellular Ca^{2+}. Over the course of the experiment,

F_{basal} remained within the standard error of F_{basal} measured under control conditions. For data analysis, transients were digitally filtered off-line (adjacent-averaging routine, smoothing factor n = 5; Origin 9.1).

Immunofluorescence

Identification of dSPNs and iSPNs

To identify SPNs of the direct (dSPN) and indirect (iSPN) pathways, neurons were filled with Neurobiotin (0.5 mg/ml, Vector Laboratories,Peterborough, United Kingdom) during recordings and subsequently processed for immunostaining of the A2A receptor (marker of iSPNs) and substance P (marker of dSPNs)(Nazzaro et al., 2012; Trusel et al., 2015). After recording, slices were fixed with 4% paraformaldehyde in 0.1 M phosphate buffer (0.1 M PB; pH 7.4) overnight at 4°C and then incubated in primary antibodies. Rabbit polyclonal antibody to A2A (1:250, Enzo Life Sciences, Farmingdale, New York) and rat monoclonal antibody to substance P (1:200, Millipore, Billerica, Massachussets) were diluted in 0.1 M PB containing 0.3% Triton X-100. Sections were subsequently incubated with Alexa 647- or Alexa 488-conjugated secondary antibodies (1:200) and Alexa 568-conjugated streptavidin (1:1000) (ThermoFisher Scientific, Carlsbad, California), mounted on glass slides, and coverslipped with ProLong Gold antifade reagent (ThermoFisher Scientific, Carlsbad, California). Images were acquired with an inverted Leica TCS SP5 AOBS TANDEM confocal microscope.

5-HT, SERT and mCherry expression

hM4Di$^{+/-}$/Pet1$_{210}$-Cre/Tph2$^{GFP+/-}$ or Pet1$_{210}$-Cre mice were perfused with 4% paraformaldehyde (w/v) in phosphate buffer (0.1 M PB; pH 7.4) and vibratome sections (50 µm) were processed for immunofluorescence (Migliarini et al., 2013). After blocking and permeabilization, slices were incubated in primary antibody diluted in PBTriton solution (0.1 M PB, 0,5% Triton X-100, 5% horse serum) [rabbit anti-RFP (1:500, Abcam, Cambridge, United Kingdom); chicken polyclonal anti-eGFP (1:1000, Abcam, Cambridge, United Kingdom); rat monoclonal anti-5-HT (1:200, Merck

Millipore, Darmstadt, Germany)] overnight at 4°C. Rabbit anti-SERT (1:500, Millipore, Darmstadt, Germany) primary antibody was diluted in modified PBTriton (0.1 M PB, 0,3% Triton X-100, 10% horse serum) and slices incubated for 36 h at 4°C. Slices were then incubated in secondary antibody [Alexa Fluor 488 goat anti-chicken IgG (1:500, Molecular Probes, Eugene, Oregon); VectaFluor™ Excel Amplified DyLight® 594 Anti-Rabbit IgG Kit; Alexa Fluor 488 donkey anti-rat IgG (1:500, Molecular Probes, Eugene, Oregon)] for 2 h at room temperature and mounted onto slides for imaging. Images were acquired with a MacroFluo microscope (Leica, Weltzar, Germany) with a DS-SMc digital camera (Nikon, Tokyo, Japan) or with an A1 confocal microscope (Nikon, Tokyo, Japan).

Postsynaptic localization of 5-HT4R in dSPNs

Labeling of cortical and thalamic afferents

To identify cortical afferents, VGLUT1-Venus knock-in mice were used and no injections were required (Heck et al., 2015; Herzog et al., 2011). To label thalamic afferents, AAV9.CAG.Flex.eGFP.WPRE.bGH (UPenn) was injected in the thalamus of VGLUT2-Cre mice (-2.3 AP; ±0.75 LM; -3.5 DV). A volume of 0.5 µl/site of virus (diluted 1:10 in PBS) was injected at a rate of 0.1 µl/min. Mice were perfused 3-4 weeks after the injection. To label dSPNs, the viral construct AAVrh9-PPTA-CRE, which contains an expression cassette consisting of Cre recombinase driven by the promoter of the PPTA gene (substance P), which is specifically expressed in dSPNs, was co-injected with AAV9.CAG.Flex.tdTomato.WPRE.bGH (UPenn) expressing "flexed" tdTomato under the CMV/actin hybrid promoter (CAG). The DLS was targeted (+0.5 AP; ±2.6 LM; -2.9 DV) and a volume of 2 µl/site of the mix was injected at a rate of 0.1 µl/min. Mice were perfused 2-3 weeks after the injection (Dos Santos et al., 2017) (Hikida et al., 2010). In VGLUT2-Cre mice, double injections of the AAVrh9-PPTA-CRE/AAV9.CAG.Flex.tdTomato.WPRE.bGH mix in the DLS and of AAV9.CAG.Flex.eGFP.WPRE.bGH in the thalamus were also performed. Mice were

perfused 3 weeks after the injection. The tdTomato- and eGFP-expressing viruses were made available by Dr. Hongkui Zeng of the Allen Institute for Brain Science.

Mouse perfusion and preparation of vibratome sections

Mice were deeply anesthetized and intracardially perfused with 4% PFA in 0.1 M phosphate buffer, pH 7.4 at 4°C. The brain was removed from the skull and placed in 4% PFA overnight at 4°C. Sections of 30 or 50 µm were cut in the frontal plane using a vibratome 1000S (Leica, Wetzlar, Germany), and stored in PBS.

Immunocytochemical labeling

Sections were permeabilized for 15 min in 0.5% Triton X-100, blocked for 1 h at room temperature in PBS containing 0.01% Triton-X-100, 3% BSA and 3% NGS. The sections were incubated 48 hours at 4°C with primary antibodies (rabbit anti-5-HT4R: 1:500, Abcam; mouse anti-bassoon: 1:250, Abcam) in PBS with 0.01% Triton-X-100, 3% BSA and 3% NGS. After washing, sections were incubated for 90 min at room temperature with secondary antibodies (goat anti-rabbit Cy3-conjugated or Cy5-conjugated; goat anti-mouse Cy5-conjugated; 1:500, Jackson) in PBS with 0.01% Triton-X-100, 3% BSA and 3% NGS. Sections were washed before mounting in Prolong Gold.

Confocal image acquisition and deconvolution

Images stacks were acquired with a Confocal Laser Scanning Microscope (SP5, Leica, Wetzlar, Germany),) through an 63x oil immersion objective with numerical aperture of 1.4 (Leica, Wetzlar, Germany) using 700Hz scanning frequency and pinhole aperture set to 1 Airy Unit. Stacks of 25 images (1024x1024 pixels) were acquired with a pixel size of 60 nm and z-step of 200 nm. Excitation (ex.) wavelength and emission (em.) range were set as follows: Venus, ex. 514, em. 545-540; GFP, ex. 488, em. 500-550; tdTomato and Cy3, ex. 561, em. 570-625; Cy5, ex. 633, em. 650-750 nm. Images were acquired in sequential mode with a low-noise Hybrid detector combining avalanche gain and GaAsP detection (HyD, Leica Wetzlar, Germany). Metrology measurements were performed on fluorescent beads to confirm proper alignment of lasers and field homogeneity, using the ImageJ-based MetroloJ plugin. Deconvolution with the experimental point spread of function from

fluorescent beads using the Maximum Likelihood Estimation algorithm was performed with Huygens software (Scientific Volume Imaging).

Image analysis

Segmentation varicosities, distance measurements and co-localization analysis were performed in three dimensions (3D) using the procedures implemented in the ImageJ-based DiAna plugin, extensively described in Gilles (Gilles et al., 2017). The 3D intensity radial distribution centered on the local maximum of each object was used to segment the objects. GFP in thalamic afferents was localized in the axons as well as in. Thus, axonal boutons were selected according to their co-localization with the immunolabeled presynaptic active zone protein Bassoon. Following segmentation, 3D distances between the borders of VGLUT objects and the closest 5-HT4R were computed and co-localizing objects counted. For co-localization analysis of 5-HT4R on spine heads and shafts, the dendritic shaft was first reconstructed with Neuronstudio software, then imported into ImageJ while spine heads were segmented in ImageJ (Dos Santos et al., 2017; Heck et al., 2015). 5-HT4R co-localization analysis was then performed with shafts and spine heads.

Immuno-EM analysis

Pre-embedding immuno-gold analyses were performed as described (Hebert-Chatelain et al., 2014). In short, after a pre-incubation step in blocking solution [(10% BSA, 0.1% sodium azide and 0.02% saponin in Tris-buffered saline (TBS)], coronal sections were incubated with rat monoclonal anti-mCherry (1:50, Sigma Aldrich Italia, Milano, Italy) and rabbit polyclonal anti-5-HT (1:200, ThermoFisher Scientific, Waltham, Massachusetts, USA) primary antibodies in blocking solution with 0.004% saponin. After several washes (1% BSA in TBS), sections were incubated with a goat anti-rabbit biotinylated secondary antibody (1:150, Vector Laboratories, Peterborough, United Kingdom) and with secondary 1.4 nm gold-labeled goat anti-rat Immunoglobulin-G (Fab' fragment, 1:100, Nanoprobes Inc., Yaphank, New York, USA). Sections were then processed in avidin-biotin complex (1:50, Vector Laboratories, Peterborough, United Kingdom), silver-intensified with the HQ

Silver kit (Nanoprobes Inc., Yaphank, New York, USA), and incubated in a solution of 0.05% DAB and 0.01% hydrogen peroxide (Vector Laboratories, Peterborough, United Kingdom). After post-fixation with 1% glutaraldehyde, the immunolabeled sections were analyzed by electron microscopy, as described (Giacomini et al., 2016). Scanning transmission electron microscopy (STEM) images were collected with a Schottky field-emission gun FEI Tecnai G2 F20 (FEI, Hillsboro, Oregon) transmission electron microscope equipped with a high angular annular dark field (HAADF) detector and operating at an acceleration voltage of 200 kV.

Activation of CaMKII in acute slices

Acute slices from drd1a-tdTomato^{tg} mice (n=3) were prepared as described (Trusel et al., 2015) After 1 h of recovery in aCSF at 32°C, slices were incubated 10 min at 32°C with or without 5 µM of the 5-HT4R agonist RS67333; after 5 min washout at 32°C in aCSF, slices were fixed in 4% PFA + 50 mM NaF for 4 h at 4°C. Slices were then rinsed three times (5 min each) in PBS and stored at -20°C in a cryoprotective solution (PBS + 30% glycerol + 30% PEG) until immunofluorescence was performed. After several washes in PBS, slices were permeabilized in PBS + 0.5% Triton-X-100 for 4 h at room temperature, blocked with PBS + 0.5% Triton-X-100 + 3% BSA for 1 h at room temperature and incubated with the primary antibody [rabbit anti-pCaMKII (Thr286) 1:400, Cell Signaling] in PBS + 0.1% Triton-X-100 + 3% BSA overnight at 4°C. After several washes in PBS, slices were incubated with the secondary antibody (Alexa 488 anti-rabbit, 1:500, ThermoFisher Scientific) in PBS + 0.1% Triton-X-100 + 3% BSA for 2 h at room temperature. After several washes in PBS, slices were mounted in ProLong Gold. Images were acquired with an inverted confocal microscope (Leica TCS SP5 AOBS TANDEM) with a 20X objective, acquiring 10 µm thick stacks with a 2 µm z-step, starting from 30 µm below the surface of the slice. For each experimental condition, 3 slices were acquired, and 2 images per slice were analyzed, counting the total number of pCaMKII and tdTomato double-positive cells.

QUANTIFICATION AND STATISTICAL ANALYSIS

Appropriate parametric statistic were utilized to test our hypothesis, unless data did not meet the assumptions of the intended parametric test (normality test). In this case, appropriate non-parametric test were used. Power analysis assumptions were: power = 0.9; alpha = 0.5; two-tailed and expected difference 50% greater than the observed standard deviation. Data were analyzed by two-way repeated measure (RM2WA) or one-way repeated measures ANOVA (RM1WA) for comparisons within a group, and one-way ANOVA (1WA) for between-group comparisons (GraphPad Prism 6 software). Post-hoc analysis (Tukey; Home-Sidak, as indicated) was performed only when ANOVA yielded a significant main effect. Two groups were tested for statistical significance using the two-population t-test and Mann-Whitney U-nonparametric test (GraphPad Prism 6 software). Statistical details of experiments are shown in results, figures and figure legends. Data are reported as mean ± s.e.m., unless stated otherwise. In the electrophysiological experiments, measurement of EPSPs were made using pClamp software (Molecular Devices). The occurrence and magnitude of synaptic plasticity was evaluated by comparing the normalized EPSP amplitudes from the last 5 min of baseline recordings with the corresponding values at 25-35 min after STDP (as indicated in **Figure 1B**). LTD plots were generated by averaging the peak amplitude of individual EPSPs in 1 min bins. Coefficients of variation (CV) for EPSPs were calculated by the ratio of the standard deviation (sd) and the mean EPSP amplitude (Shen et al., 2008). In imaging experiments, the magnitude of the Ca^{2+} signal was measured as the area under the curve (AUC) in the transient region. n values for electrophysiological and imaging experiments represent the number of recorded cells. No statistical methods were used to pre-determine sample sizes, which were, however, similar to those reported previously (Nazzaro et al., 2012; Trusel et al., 2015). For immunohistochemistry, images were processed with Adobe Photoshop (Adobe Systems) using only linear adjustments of contrast and color.

DATA AND SOFTWARE AVAILABILITY

Mouse strains:

Pet1$_{210}$-Cre; MGI:5620670 [http://www.informatics.jax.org/allele/key/854058]

Mouse Tph2GFP$^{+/-}$; MGI:5442736 [http://www.informatics.jax.org/allele/key/821477]

A custom macro in ImageJ using algorithms from the Plugin 3DImageSuite (http://imagejdocu.tudor.lu/doku.php?id=plugin:stacks:3d_ij_suite:start) is available upon request (nicolas.heck@upmc.fr) since it requires to be adapted according to image names and calibration.

KEY RESOURCES TABLE

REAGENT or RESOURCE	SOURCE	IDENTIFIER
Antibodies		
Rabbit polyclonal antibody to A2A	Enzo Life Sciences	Cat# BML-SA654; RRID: AB_2226507
Rat monoclonal antibody to substance P	Millipore	Cat# MAB356; RRID: AB_94639
Alexa 488 anti-rabbit	ThermoFisher Scientific	Cat# A-11034; RRID: AB_2576217
Alexa 647 anti-rat	ThermoFisher Scientific	Cat# A-21247; RRID: AB_141778
Rabbit anti-RFP antibody	AbCam	Cat# ab62341; RRID: AB_945213
Chicken polyclonal anti-eGFP	AbCam	Cat# ab13970; RRID: AB_300798
Rat monoclonal anti-5HT	Millipore	Cat# MAB352 RRID: AB_94865
Alexa Fluor 488 goat anti-chicken IgG	Molecular Probes	Cat# A-11039; RRID: AB_142924
VectaFluor™ Excel Amplified DyLight® 594 Anti-Rabbit IgG Kit	Vector Laboratories	Cat# DK-1594; RRID: AB_2336778
Alexa Fluor 488 donkey anti-rat IgG	Molecular Probes	Cat# A-21208; RRID: AB_141709
Rabbit anti-5-HT4R	AbCam	Cat# ab60359; RRID: AB_2122438
Mouse anti-bassoon	AbCam	Cat# ab82958; RRID: AB_1860018
Goat anti-rabbit Cy3-conjugated	Jackson	Cat# 111-165-003; RRID: AB_2338000
Goat anti-rabbit Cy5-conjugated	Jackson	Cat# 111-175-144; RRID: AB_2338013
Goat anti-mouse Cy5-conjugated	Jackson	Cat# 115-175-205; RRID: AB_2338715
Rat monoclonal anti-mCherry	ThermoFisher Scientific	Cat# M11217; RRID: AB_2536611

Rabbit polyclonal anti-5HT	ThermoFisher Scientific	Cat# PA1-36157; RRID: AB_1087251
Rabbit polyclonal anti-SERT	Millipore	Cat# AB9726; RRID: AB_612176
Goat anti-rabbit biotinylated secondary antibody	Vector Laboratories	Cat# BA-1000; RRID: AB_2313606
1.4 nm gold-labeled goat anti-rat Immunoglobulin-G (Fab' fragment)	Nanoprobes	Cat# 2008; RRID N/A
Alexa 568-conjugated streptavidin	ThermoFisher Scientific	Cat# S-11226; RRID: AB_2315774
Rabbit anti-pCaMKII (Thr286)	Cell Signaling Technology	Cat# 3361; RRID: AB_10015209
Bacterial and Virus Strains		
rAAV5-CaMKIIa-ChR2(H134R)-eYFP	UNC Vector Core	AV4316O
rAAV5-EF1a-DIO-hChR2(H134R)-eYFP	UNC Vector Core	AV4313X
AAV9.CAG.Flex.eGFP.WPRE.bGH	Upenn, Dr. Hongkui Zeng	AV-9-ALL854
AAVrh9-PPTA-cre.WPRE	Laboratory of Dr. J. Caboche	N/A
AAV9.CAG.Flex.tdTomato.WPRE.bGH	Upenn, Dr. Hongkui Zeng	AV-9-ALL864
Biological Samples		
Chemicals, Peptides, and Recombinant Proteins		
Fluo-4	ThermoFisher Scientific	Cat# F14200
Alexa Fluor 568 Hydrazide	ThermoFisher Scientific	Cat# A10437
Neurobiotin	Vector Laboratories	Cat# SP-1120; RRID: AB_2313575
ProLong Gold AntiFade reagent	ThermoFisher Scientific	Cat# P36935
SR95531	Tocris Bioscience	Cat# 1262; CAS Number: 104104-50-9
SB271046	Tocris Bioscience	Cat# 3368; CAS Number: 209481-24-3
GR113808	Tocris Bioscience	Cat# 1322; CAS Number: 144625-51-4
RS39604	Tocris Bioscience	Cat# 0991; CAS Number: 167710-87-4
AM251	Tocris Bioscience	Cat# 1117; CAS Number: 183232-66-8

Paxilline	Tocris Bioscience	Cat# 2006; CAS Number: 57186-25-1
RS67333	Tocris Bioscience	Cat# 0989; CAS Number: 168986-60-5
AIP	Tocris Bioscience	Cat# 1688; CAS Number: 167114-91-2
PKI 5-24	Tocris Bioscience	Cat# 6221; CAS Number: 99534-03-9
KN-62	Tocris Bioscience	Cat# 1277; CAS Number: 127191-97-3
R-CPP	Tocris Bioscience	Cat# 2334; CAS Number: 126453-07-4
D15	Tocris Bioscience	Cat# 2334; CAS Number: 251939-41-0; Sequence: PPPQVPSRPNRAPPG
S15	TermoFisher Scientific	Sequence: ANVRRGPPPPPQPSP
GluA23Y	TermoFisher Scientific	Sequence: YKEGYNVYG
GluA23Y Scramble (GluA23A)	TermoFisher Scientific	Sequence: AKEGANVAG
CNO (Clozapine-N-Oxide)	Sigma Aldrich	C0832; CAS Number: 34233-69-7
Critical Commercial Assays		
HQ Silver kit	Nanoprobes	Cat# 2012
avidin-biotin complex	Vector Laboratories	Cat# PK-6100; RRID: AB_2336819
Deposited Data		
Analyzed Data	This paper	N/A
Experimental Models: Cell Lines		
Mouse: ES cells	BayGenomics	E14Tg2a.4
Experimental Models: Organisms/Strains		
Mouse: C57BL/6J	Charles River	C57BL/6J; RRID: IMSR_JAX:000664
Mouse: hM4Di$^{+/-}$/Pet1$_{210}$-Cre	Laboratory of Prof. Massimo Pasqualetti	N/A
Mouse: hM4Di$^{+/-}$/Pet1$_{210}$-Cre^{0}	Laboratory of Prof. Massimo Pasqualetti	N/A
Mouse: Pet1$_{210}$-Cre	Laboratory of Prof. Massimo Pasqualetti	N/A

Mouse: B6.Cg-Tg(Thy1-COP4/EYFP)18Gfng/J	The Jackson Laboratory	Cat# JAX:007612; RRID: IMSR_JAX:007612
Mouse: hM4Di$^{+/-}$/Pet1$_{210}$-Cre/Tph2$^{GFP+/-}$	Laboratory of Prof. Massimo Pasqualetti	N/A
Mouse: *Drd1a*-td Tomato BAC transgenic mouse line 5, and backcrossed to C57BL/6J	Laboratory of Dr. N.Calakos	N/A
Mouse: VGLUT1^{Venus} knock-in	Laboratory of Dr. Etienne Herzog; Laboratory of Dr. J. Caboche	N/A
Mouse: Slc17a6$^{tm2(cre)Lowl}$/J (VGLUT2-Cre)	The Jackson Laboratory	Cat# 016963; RRID: IMSR_JAX:016963
Oligonucleotides		
Primer: wild-type *ROSA26* allele forward 5'-GAGGGGAGTGTTGCAATACC-3'	BMR Genomics	N/A
Primer: wild-type *ROSA26* allele reverse 5'-AGTCTAACTCGCGACACTGTA-3'	BMR Genomics	N/A
Primer: reverse 5'-GTCCCTATTGGCGTTACTATG-3'	BMR Genomics	N/A
Recombinant DNA		
Plasmid: pCX-CAG-*eGFP*	Pasqualetti et al, Genesis 2002	doi: 10.1002/gene.10053
Plasmid: pROSA26-1^{Sor}	Soriano P. Nat Genet. 1999	AddGene: #21714; doi: 10.1038/5007
Plasmid: pPSVKeoFRT	Pasqualetti et al, Genesis 2002	doi: 10.1002/gene.10053
Vector: pROSA26-1^{Sor}-CAG-*hM4Di/mCherry*	This paper	N/A
Plasmid: pAAV-hSyn-DIO-*hM4Di/mCherry*	Krashes et al, J Clin Invest. 2011	AddGene: #44362; doi:10.1172/JCI46229.
Software and Algorithms		
GraphPad Prism 6 software	GraphPad Software, Inc.	https://www.graphpad.com/ ; RRID: SCR_002798
pClamp 10	Molecular Devices	http://mdc.custhelp.com/ ; RRID: SCR_011323
ImageJ	NIH	http://rsb.info.nih.gov/ij/ ; RRID: SCR_003070

Neuronstudio software	Computational Neurobiology and Imaging Center	http://research.mssm.edu/cnic/tools-ns.html ; RRID: SCR_013798
Huygens software (Maximum Likelihood Estimation algorithm)	Scientific Volume Imaging	https://svi.nl/HuygensSoftware ; RRID: SCR_014237
Origin 9.1	OriginLab Corporation	https://store.originlab.com/store/Default.aspx?CategoryID=0 ; RRID: SCR_014212
Adobe Photoshop CS6	Adobe Systems	https://www.adobe.com/ ; RRID: SCR_014199
Other		
AN69 dialyzing membranes	Hospal Dasco	Nephral ST 500

Figure 1

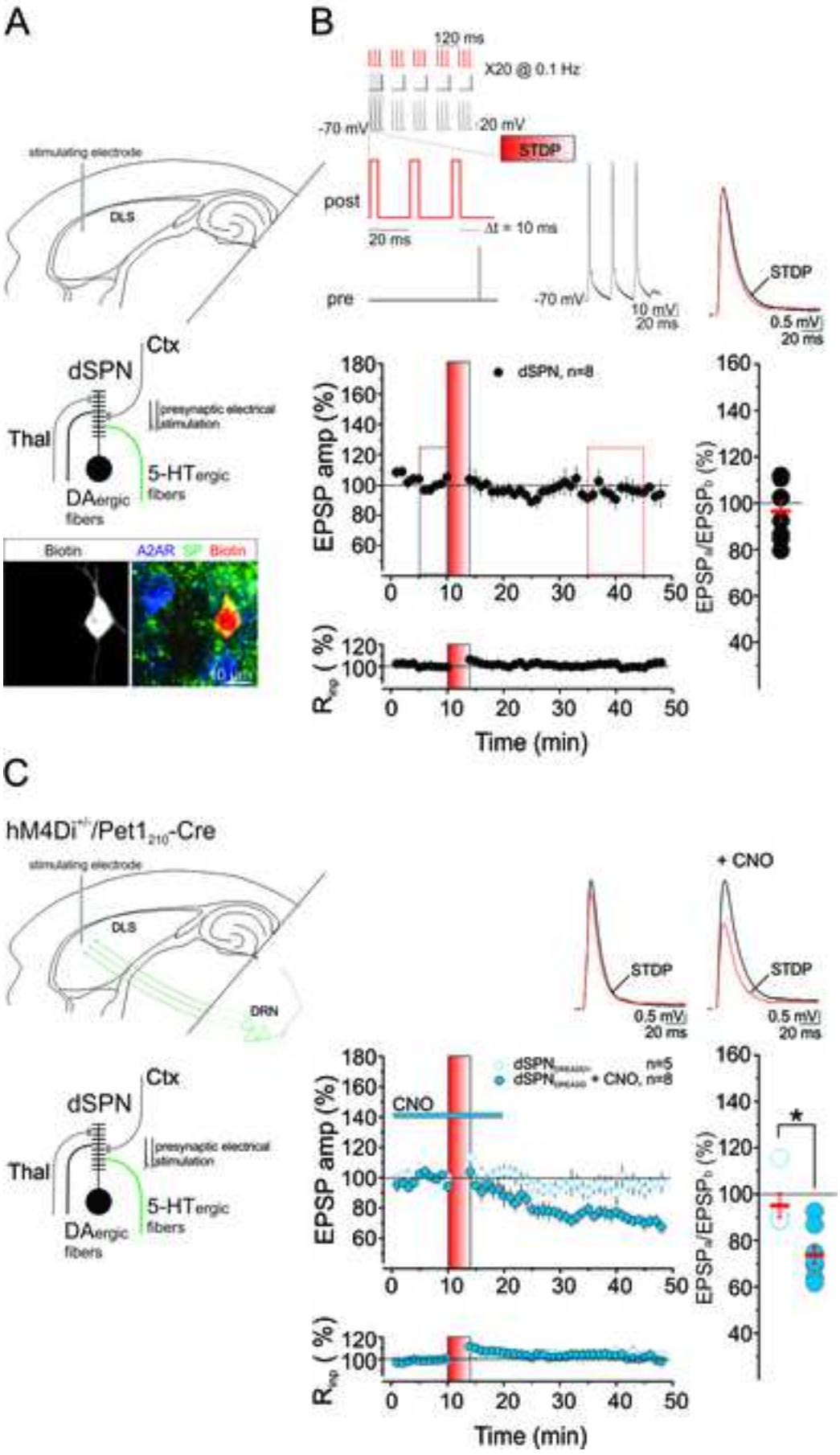

Figure

Click here to download Figure Figure 2_5HT_R2.tif

Figure 2

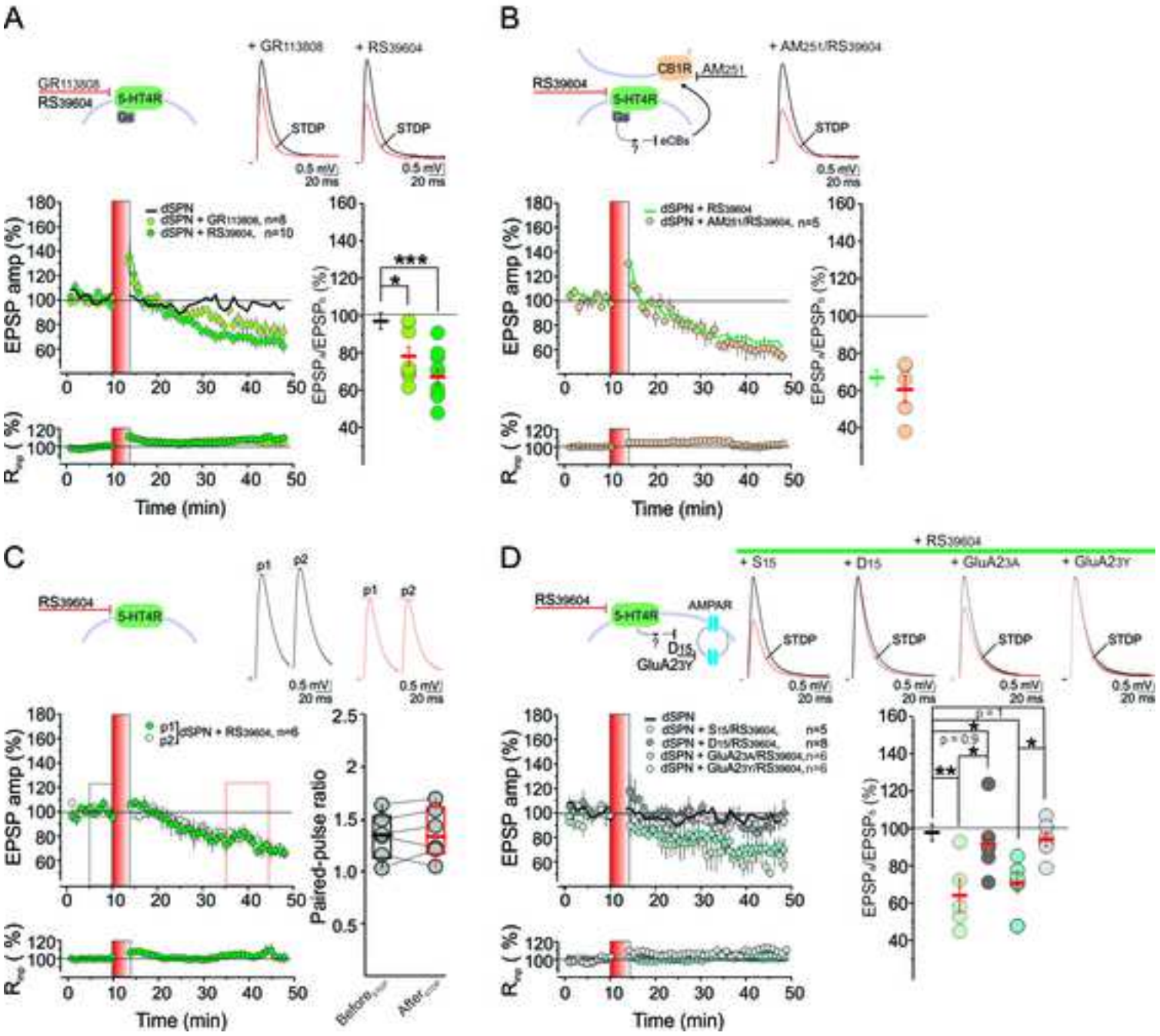

Figure

Click here to download Figure Figure 3_5HT_R2.tif

Figure 3

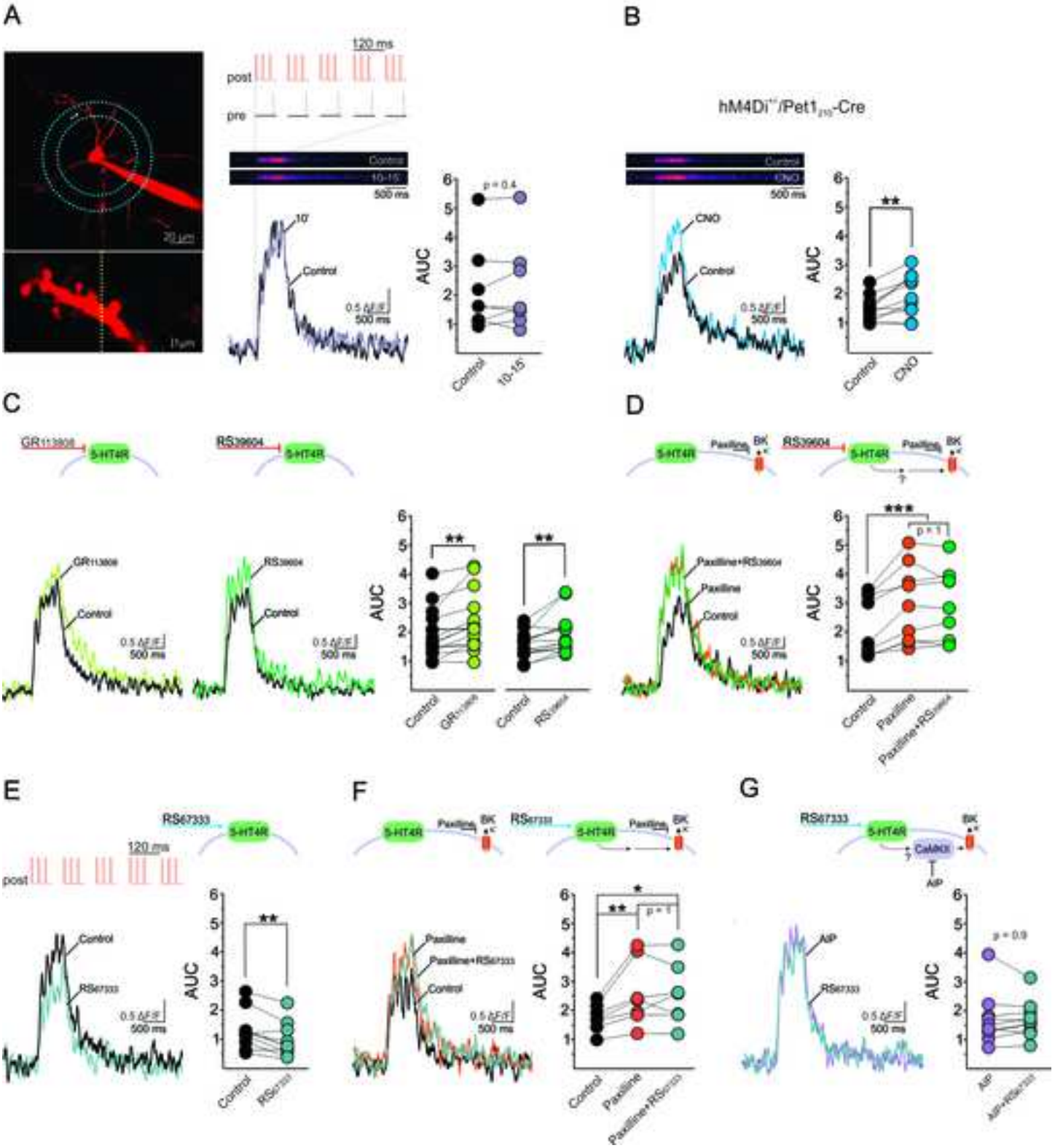

Figure 4

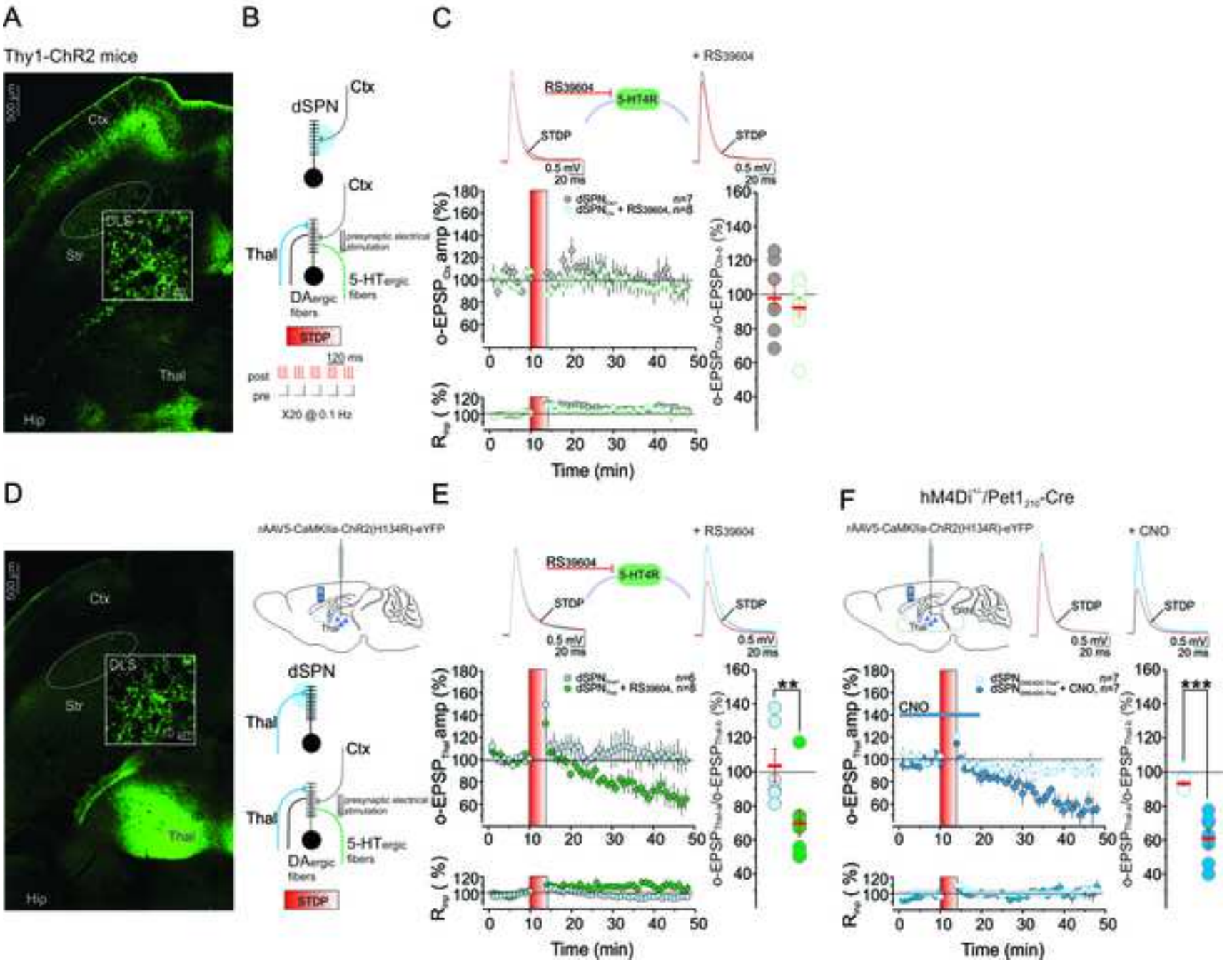

Figure

Click here to download Figure Figure 5_5HT_R2.tif

Figure 5

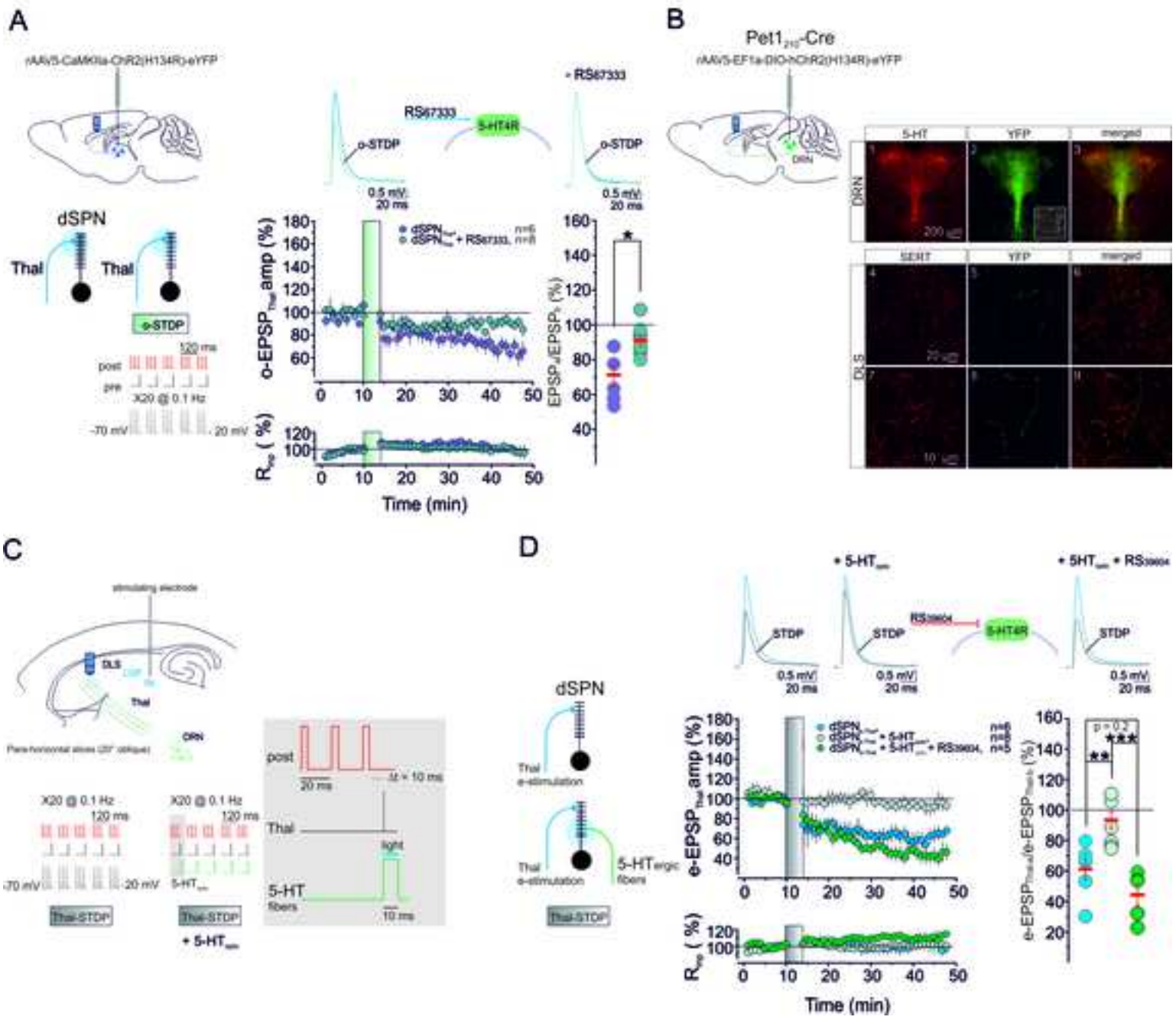

Figure 6

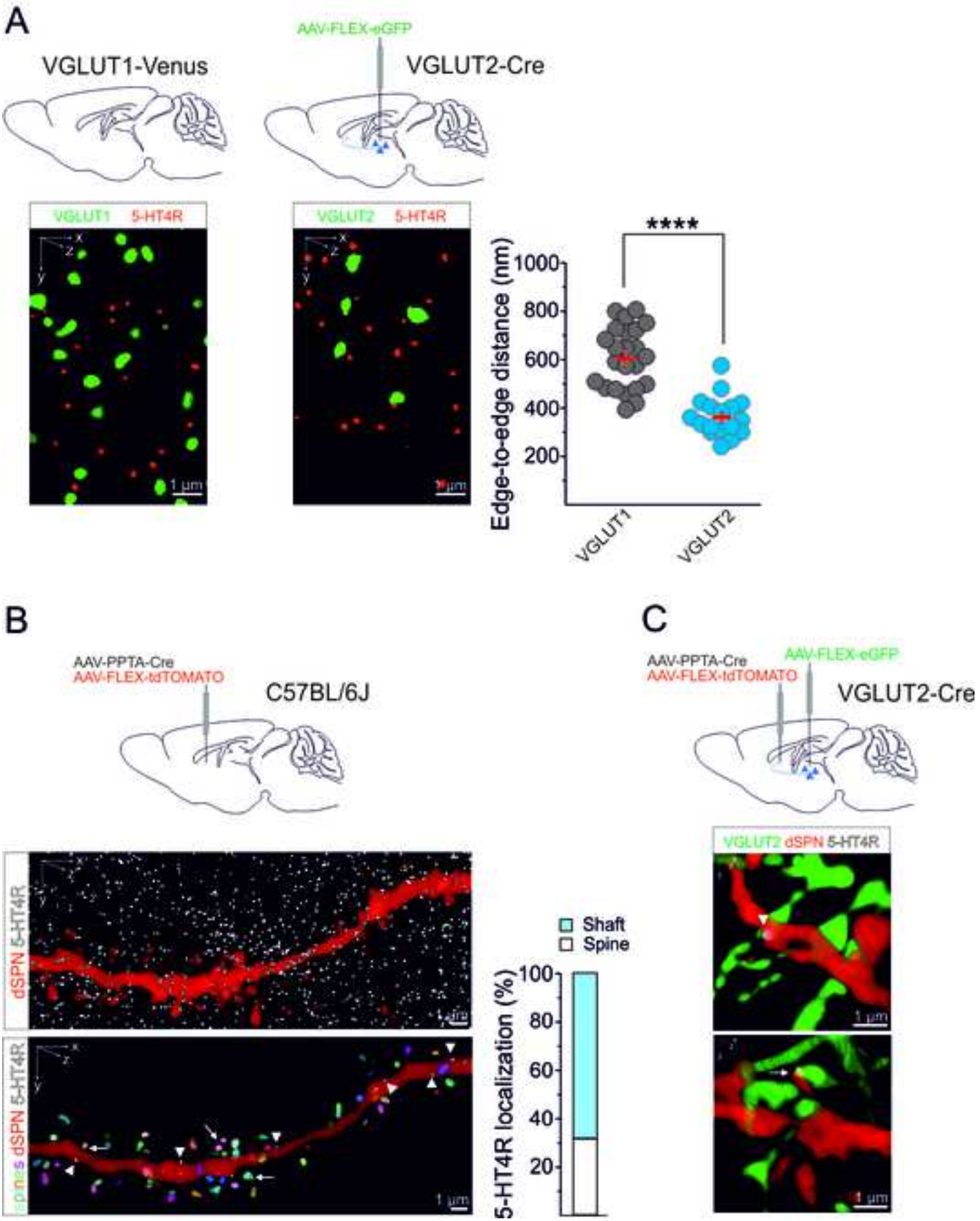

Figure

Click here to download Figure Figure 7_5-HT_R2.tif

Figure 7

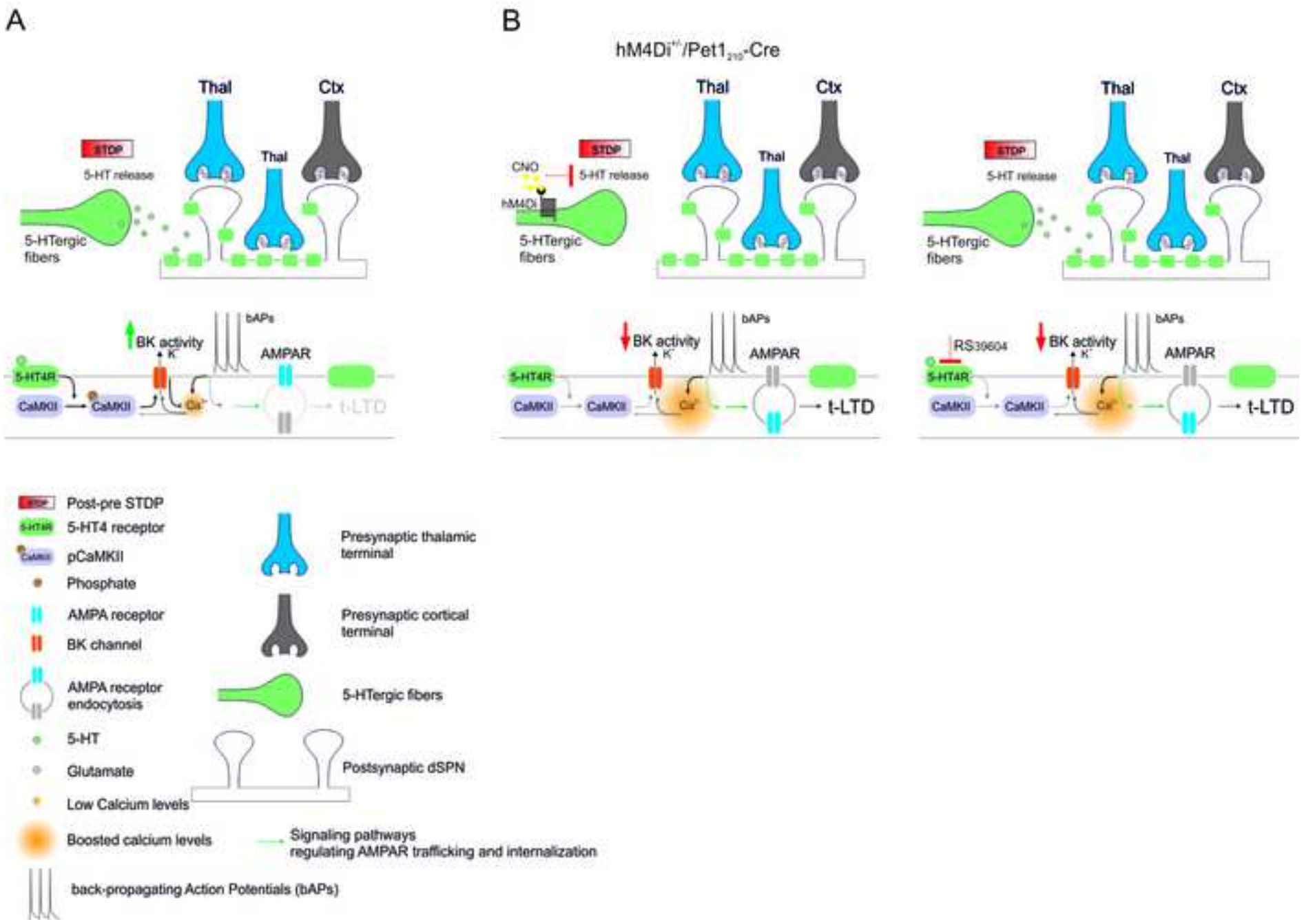

Figure S1

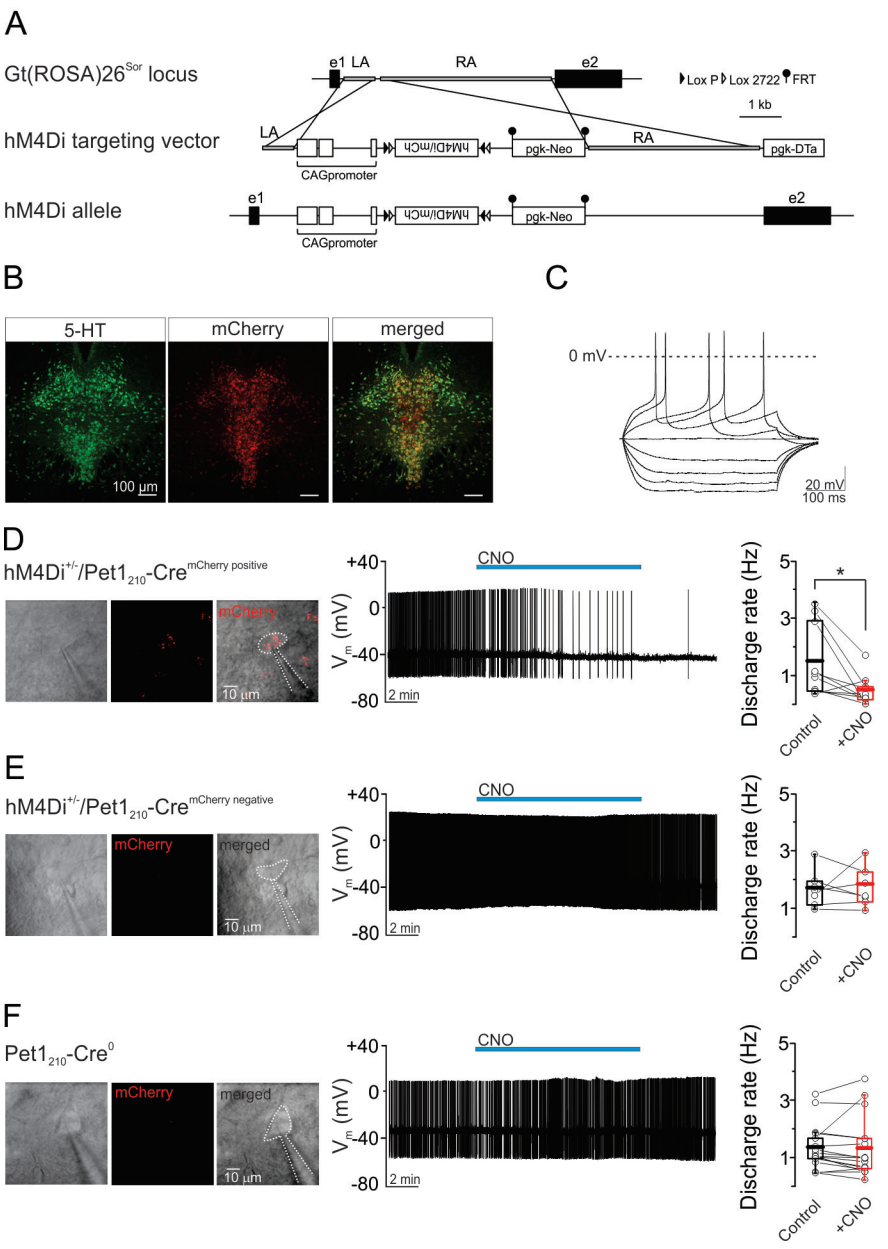

Figure S1, related to Figure 1. hM4Di conditional knock-in mouse line

(**A**) Schematic of construct used to generate the hM4Di conditional knock-in mouse line. From top to bottom: the genomic structure of the ROSA26 locus with the homology regions highlighted that were used to prepare the hM4Di targeting vector, and the resulting hM4Di recombined conditional knock-in allele. LA: left homology arm; RA right homology arm; e1: exon 1; e2: exon 2; pgk-Neo: neomycin expression cassette containing the phosphoglycerate-kinase promoter and neomycin coding sequence; pgk-DTa: diphtheria toxin A expression cassette containing the phosphoglycerate-kinase promoter and diphtheria toxin A coding sequence; hM4Di/mCh: in-frame fusion protein resulting from the hM4Di DREADD receptor and the mCherry reporter coding sequences. (**B**) Double immunofluorescence analysis. Confocal images showing expression of 5-HT (green), mCherry (red) and merge in dorsal raphe nuclei (DRN) of hM4Di$^{+/-}$/Pet1$_{210}$-Cre mice. Scale bar, 100 µm. (**C**) DRN 5-HT neurons were identified on the basis of their current-clamp electrophysiological profile, including the lack of time-dependent depolarization (sag) in response to hyperpolarizing current pulses (400 ms long). (**D, E**) (Left and middle) In acute DRN brain slices from hM4Di$^{+/-}$/Pet1$_{210}$-Cre mice, activation of the inhibitory DREADD receptor hM4Di by clozapine-N-oxide (CNO; 5 µM) decreased the firing rate of mCherry^{positive} 5-HT neurons (**D**) but not of mCherry^{negative} 5-HT neurons (**E**). (**F**) (Left and middle) CNO had no effect in 5-HT neurons of Pet1$_{210}$-Cre^{0} littermate animals. (**D-F**) (Right) Box-plot summary of the changes in discharge rate in response to bath application of CNO in mCherry^{positive} neurons (**D**; control, 1.48 ± 0.40 Hz; CNO, 0.49 ± 0.16 Hz; n = 10, 5 mice, *p< 0.05, paired t-test) and mCherry^{negative} neurons (**E**; control, 1.72 ± 0.24 Hz; CNO, 1.77 ± 0.26 Hz; n = 7, 3 mice, p = 0.9, paired t-test) of hM4Di$^{+/-}$/Pet1$_{210}$-Cre mice and Pet1$_{210}$-Cre^{0} littermate animals (**F**; control, 1.34 ± 0.19 Hz; CNO, 1.30 ± 0.26 Hz; n = 17, 8 mice, p = 0.8, paired t-test). Values are the minimum, mean (bar inside the box), and the maximum.

Figure S2

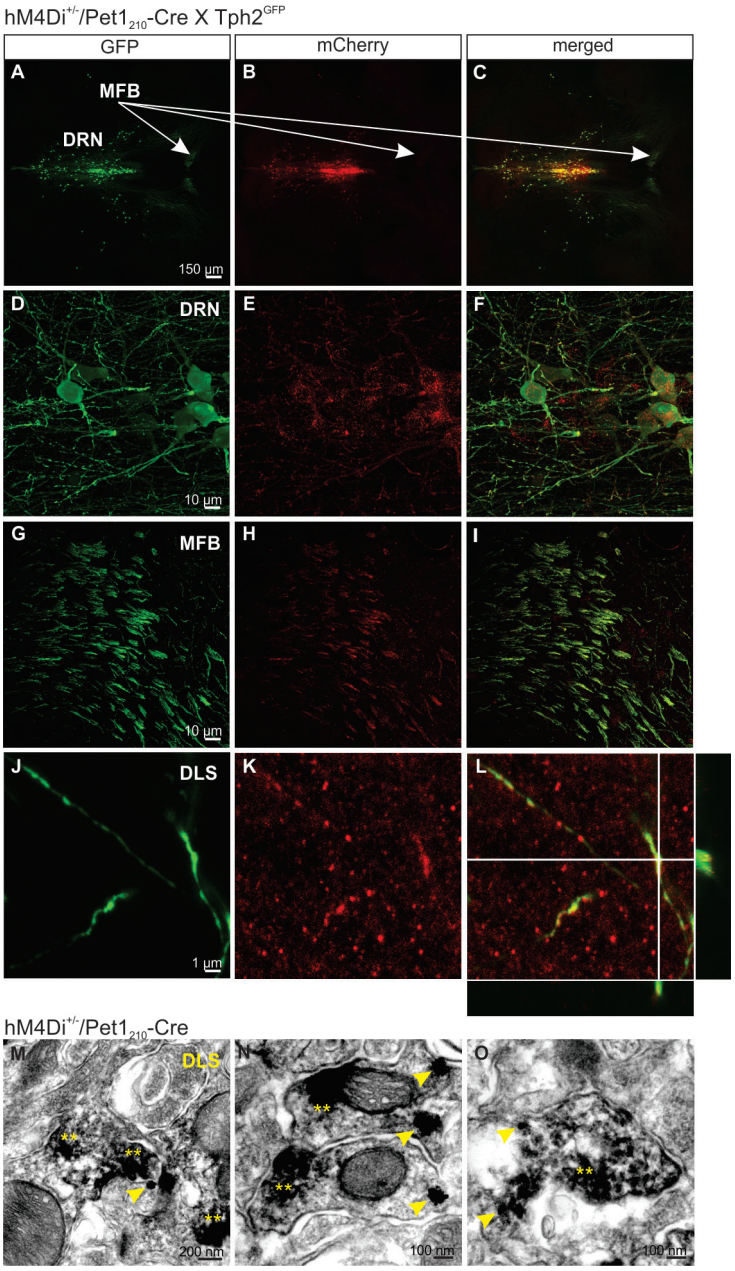

Figure S2, related to Figure 1. Expression of the hM4Di-mCherry receptor in DRN neurons and 5-HT fibers

(**A-C**) Confocal microscopy images of horizontal brain sections of mice generated by crossing the hM4Di$^{+/-}$/Pet1$_{210}$-Cre mouse line with Tph2$^{GFP+/-}$ mice (Migliarini et al., 2013). Immunostaining for GFP and mCherry reveals the expression of the fluorescent reporters in the adult serotonergic system. (**D-F**) High magnification confocal images confirming the presence of hM4Di-mCherry fusion protein and GFP in serotonergic neurons of the DRN, (**G-I**) in the serotonergic fibers of the MFB and (**J-L**) in the DLS of hM4Di$^{+/-}$/Pet1$_{210}$-Cre/Tph2$^{GFP+/-}$mice. (**L**) Orthogonal views confirm the co-localization of mCherry and GFP in serotonergic fibers (29 Z-steps at 0.3 µm intervals). (**M-O**) Axon fibers containing 5-HT-labeling (scattered material, yellow asterisk) and mCherry-labeling (gold particles, yellow arrowhead) in the DLS of hM4Di$^{+/-}$/Pet1$_{210}$-Cre mice. Scale bars: **A-C**, 150 µm; **D-I**, 10 µm; **J-L**, 1 µm; **M**, 200 nm; **N-O**, 100 nm. MFB, medial forebrain bundle; DRN, dorsal raphe nucleus; DLS, dorsolateral striatum.

Figure S3

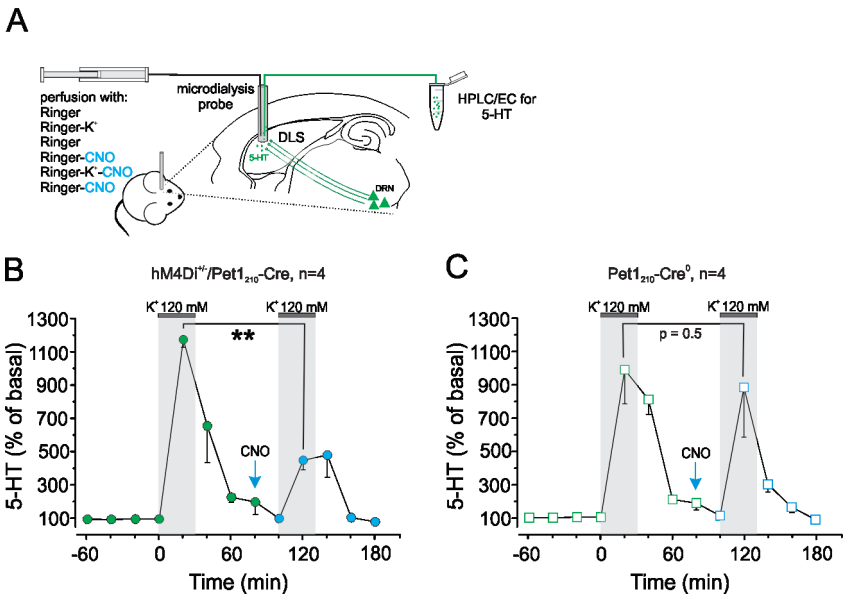

Figure S3, related to Figure 1. In vivo chemogenetic inhibition of evoked 5-HT release in the DLS of freely-moving mice

(**A**) Schematic represents microdialysis experiments in hM4Di$^{+/-}$/Pet$_{210}$-Cre mice or control littermates, which do not express the inhibitory hM4Di receptor. Infusion of CNO in the DLS reduced high-K^{+}-induced 5-HT overflow in hM4Di$^{+/-}$/Pet$_{210}$-Cre mice (**B**; n = 4 mice; RM1WA $F_{3,12}$=16 p = 0.02, 20 min versus 120 min, **p < 0.01, Home-Sidak), but not in control animals (**C**; n = 4 mice; RM1WA $F_{3,12}$= 11 p = 0.04, 20 min versus 120 min, p = 0.5, Home-Sidak).

Figure S4

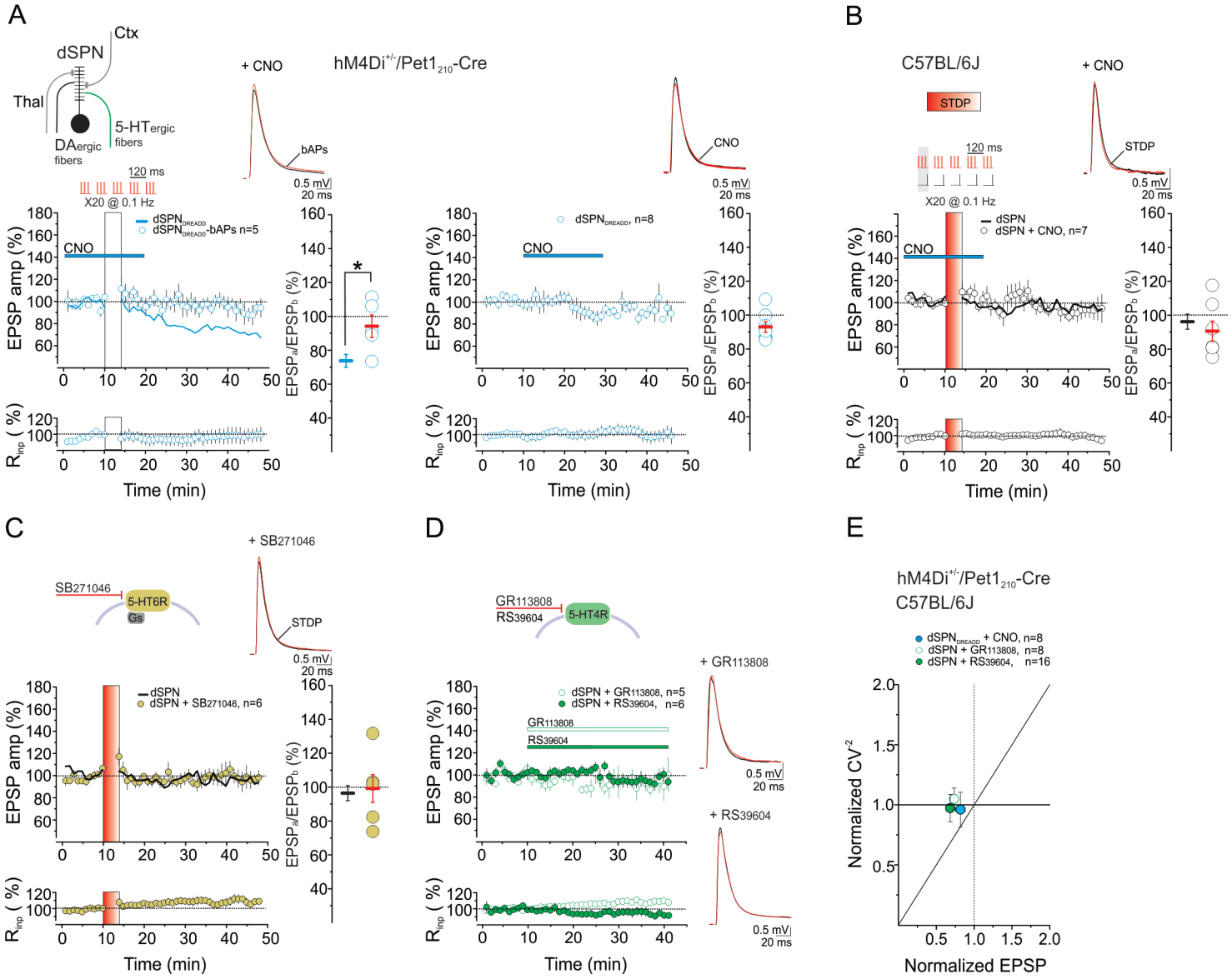

Figure S4, related to Figure 1 and Figure 2. t-LTD at glutamatergic dSPN synapses

(**A**) In hM4Di$^{+/-}$/Pet$_{210}$-Cre mice, application of CNO (5 μM, blue bar) affects neither EPSPs in response to a burst pattern of bAPs (n = 5, 3 mice; RM1WA $F_{4,44}$ = 0.9 p = 0.4; dSPN-bAPs versus dSPN-STDP, *p < 0.05, Mann Whitney test; left) nor basal EPSP responses (n = 8, 6 mice; RM1WA $F_{7,45}$ = 1.4, p = 0.3; right). (**B**) In naïve mice, application of CNO during STDP does not affect glutamatergic dSPN synapses (dSPN + CNO, n = 7, 5 mice; RM1WA $F_{6,44}$ = 1.5, p = 0.2; dSPN + CNO versus dSPN, p = 0.5, Mann-Whitney test). (**C**) The post-pre pairing protocol did not trigger plasticity in the presence of the 5-HT6R antagonist SB271046 (5 μM; n = 6, 4 mice; RM1WA $F_{5,44}$ = 1, p = 0.4; dSPN + SB271046 versus dSPN, p = 0.9, Mann Whitney test). (**A-C**) (Left) Plots show the time course of normalized EPSP amplitudes and normalized Rinp (mean ± s.e.m.). Solid blue (**A**) and black (**B**) lines (average) are the time course from **Figure 1C** and **Figure 1B**, respectively, and reported here for comparison. (Insets, left) Recording configuration (**A**, **B**) and proposed 5-HT receptor subtype targeted by SB271046 (**C**). (Insets, right) Averaged recordings (ten traces) before (black line) and after (red line) the delivery of burst pattern of bAPs (**A**, Left; white vertical bar), CNO application alone (**A**, Right), or the STDP protocol (**B**; red vertical bar). (Right) Plots summarize the ratios of synaptic responses after (a) and before (b) the different types of stimulation. (**D**) In the absence of coordinated postsynaptic and presynaptic activity, antagonism of 5-HT4R by GR113808 (5 μM) or RS39604 (5 μM) did not gate LTD (GR113808, n = 5, 4 mice; RM1WA $F_{4,40}$ = 0.7, p = 0.6; RS39604, n = 6, 3 mice; RM1WA $F_{5,40}$ = 1, p = 0.4). (Top), Schematic of proposed 5-HT receptor subtype targeted by the defined antagonists; (Insets, right) Averaged recordings (ten traces) before (black line) and 25 min after (red line) the application of GR113808 (white bar) or RS39604 (green bar). Data are presented as normalized EPSP amplitudes and normalized Rinp (mean ± s.e.m.). (**E**) Variance analysis of dSPN EPSPs suggests that t-LTD gated by decreased excitatory 5-HT signaling is expressed postsynaptically. Normalized CV^{-2} is plotted as a function of normalized EPSPs. The variation in EPSP amplitude was unchanged after t-LTD induced by the post-paring paradigm delivered in the presence of CNO (5 μM; hM4Di$^{+/-}$/Pet$_{210}$-Cre mice) or the 5-HT4R antagonists GR113808 or RS39604 (5 μM; naïve mice).

Figure S5

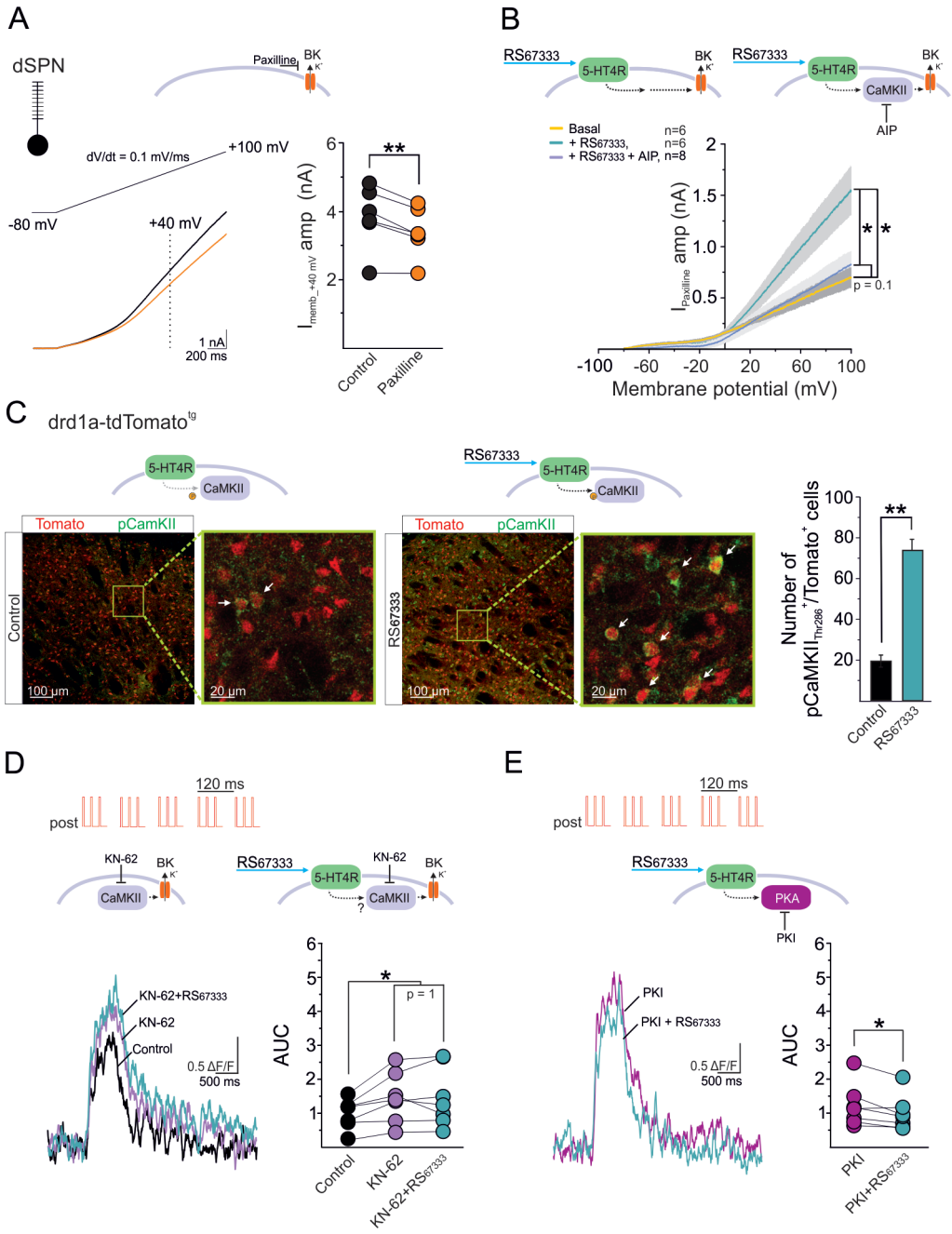

Figure S5 related to Figure 3. 5-HT4R activation positively modulates BK-mediated current and bAP-evoked Ca^{2+} transients in dSPNs through CaMKII activation

(**A**) The BK channel blocker paxilline (10 µM) reduces the outward current (I_{memb}) generated by a depolarizing ramp protocol (n = 6, 4 mice; control versus paxilline **p < 0.01, paired t-test), thus revealing a paxilline-sensitive component ($I_{Paxilline}$) in dSPNs. Sample traces (left) and scatterplot (right) show I_{memb} before and after the application of paxilline. I_{memb} amplitude was calculated at + 40 mV. (**B**) The 5-HT4R agonist RS67333 (5 µM) significantly increased $I_{Paxilline}$. This effect was prevented by the intracellular application of the CaMKII inhibitor AIP (10 µM) (n = 6-8, 6 mice per group; RM2WA voltage effect $F_{720,12240} = 101$, p < 0.0001, treatment effect $F_{2,17} = 5$, p = 0.02, interaction $F_{1440,12240} = 8$, p < 0.0001; basal versus RS67333, *p < 0.05; basal versus RS67333 + AIP, p = 1; RS67333 versus RS67333 + AIP, *p < 0.05; Tukey). (**A-B**) Inset, schematic of proposed signaling elements (**C**) 5-HT4R stimulation by RS67333 promotes phosphorylation of CaMKII in DLS dSPNs from drd1a-tdTomato^{tg} mice (n = 3). (Top) Schematics represent the proposed signaling pathway. (Bottom) Confocal laser scanning immunofluorescence detection of phosphorylation of CaMKII at Thr286 in Tomato^{+} cells (dSPNs) before (control) and in response to 5-HT4R stimulation by the agonist RS67333 (5 µM); (left-middle) representative images (scale bars, 100 µm and 20 µm) and (right) quantification (vehicle, 19 ± 3; RS67333, 74 ± 5; n = 6, **p < 0.01, Mann-Whitney test). dSPNs (Tomato^{+}) in red, pCaMKII in green. Data are presented as mean ± s.e.m. (**D-E**) (Left) bAP-induced Ca^{2+} transients, before and after a specific pharmacological manipulation, as indicated. (Right) Plot summary of modulation of evoked dendritic Ca^{2+} elevations measured as area under the curve (AUC) of the fluorescence transients. (**D**, n = 7, 4 mice; RM1WA, $F_{6,2} = 5$ p = 0.02, KN-62 versus control, *p < 0.05; KN-62 + RS67333 versus control, *p < 0.05; KN-62 versus KN-62 + RS67333, p =1; **E**, n = 7, 3 mice; PKI versus PKI + RS67333 *p< 0.05, paired t-test).

Figure S6

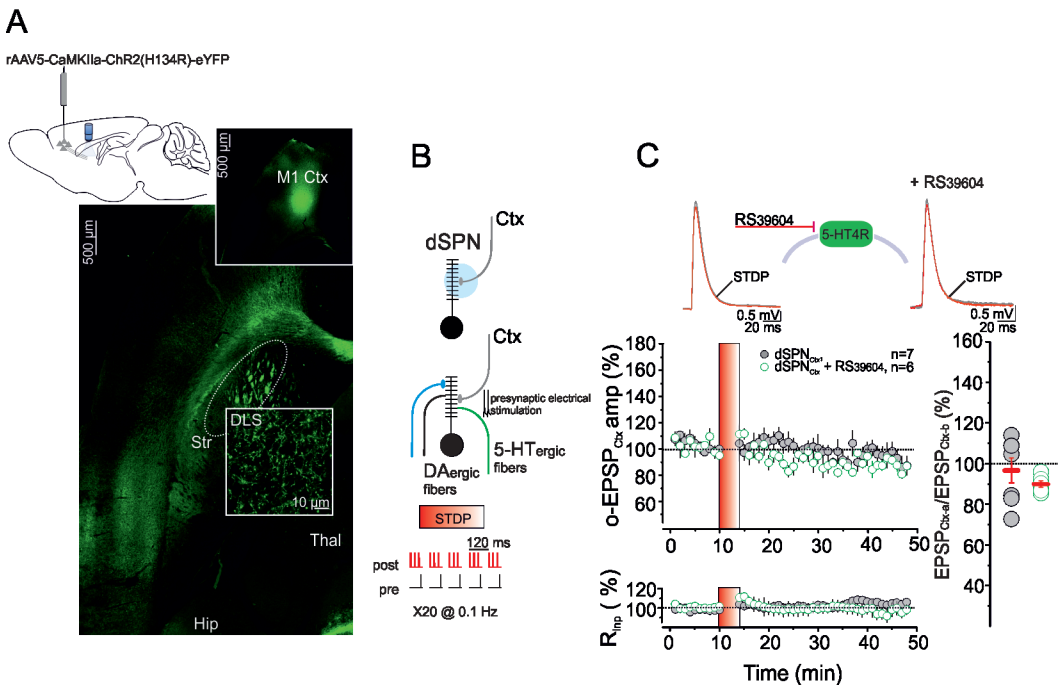

Figure S6, related to Figure 4. 5-HT4R antagonism does not gate DLS t-LTD at cortico-dSPN synapses of mice virally expressing ChR2 in the motor cortex M1

(**A**) Confocal images of horizontal sections; scale bar, 500 µm; M1 Ctx, motor cortex M1; Str, striatum; Hip, hippocampus; Thal, thalamus. Insets show the expression of ChR2-eYFP at the site of injection (M1; scale bar, 500 µm) and ChR2-eYFP expressing axon terminals in the DLS; scale bar, 10 µm. (**B**) Schematic of recording configuration in dSPNs. (**C**) The post-pre STDP protocol failed to induce plasticity of o-EPSP$_{Ctx}$ either under control conditions (dSPN$_{Ctx}$, n = 7, 4 mice; RM1WA $F_{6,44} = 1.2$, p = 0.1) or upon RS39604 application (dSPN$_{Ctx}$ + RS39604, n = 6, 6 mice; RM1WA $F_{5,44} = 3$, p = 0.06). Data are shown as time-courses (mean ± s.e.m.) of normalized EPSP amplitudes and normalized Rinp. (Insets) Averaged recordings (ten traces) before (grey line) and after (red line) the delivery of the STDP protocol (red vertical bar). Scatterplot summarizes the ratios of synaptic responses after (a) and before (b) the STDP.

Figure S7

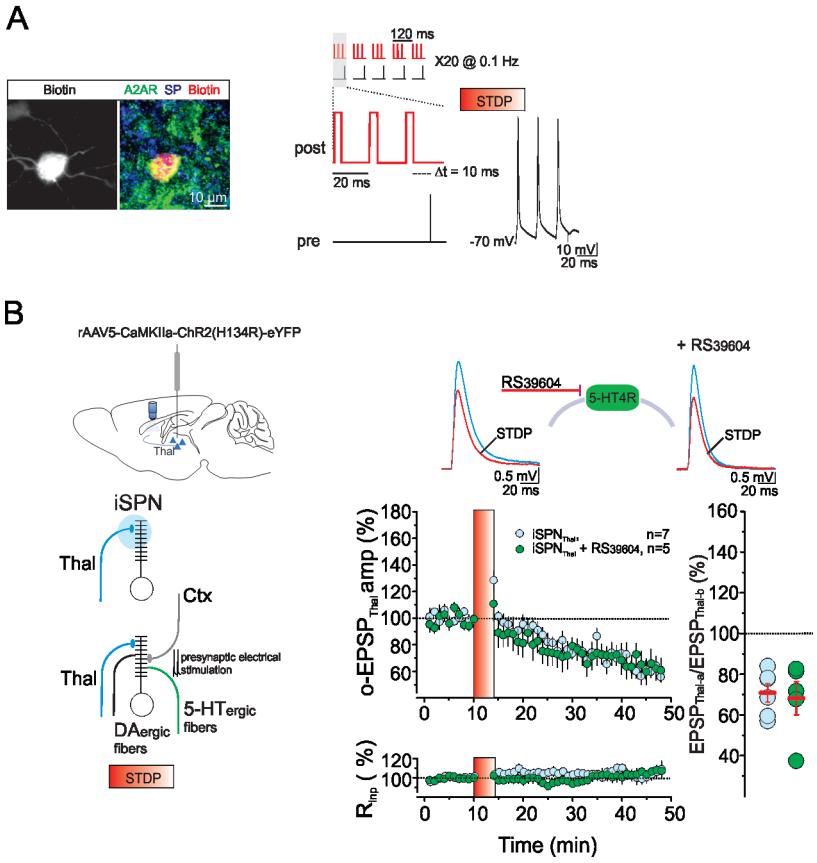

Figure S7, related to Figure 4. 5-HT4R antagonism does not affect t-LTD at thalamostrial synapses on iSPNs

(A) (Left) Confocal laser scanning microscopy images of triple immunofluorescence for adenosine A2A receptor (A2AR), substance P (SP) and biotin in patched recorded neurons (scale bar, 10 µm). (Right) The post-pre pairing protocol for the induction of t-LTD. (**B**) (Left) Schematic shows recording configurations in iSPNs. Optogenetic stimulation of thalamic afferents was performed before and after the STDP protocol. (Bottom) During the post-pre STDP paradigm, light stimulation was replaced by local electrical stimulation. (Right) In thalamic ChR2-expressing mice, the post-pre STDP protocol triggers t-LTD of iSPN o-EPSP$_{Thal}$ in either control conditions or following RS39604 application (5 µM; iSPN$_{Thal}$, n = 7, 5 mice; RM1WA $F_{6,44}$ = 12, $p < 0.0001$, $p < 0.05$ Tukey; iSPN$_{Thal}$ + RS39604, n = 5, 3 mice; RM1WA $F_{4,44}$ = 5, $p = 0.04$, $p < 0.05$ Tukey; iSPN$_{Thal}$ versus iSPN$_{Thal}$ + RS39604, $p = 0.9$, Mann-Whitney test). Data are time-courses (mean ± s.e.m.) of normalized EPSP amplitudes and normalized Rinp; scatterplot summarizes the ratios of synaptic responses after (a) and before (b) STDP. (Insets) Averaged recordings (ten traces) before (blue line) and after (red line) the delivery of the STDP (red vertical bar); schematic represents the proposed signaling pathway.

Figure S8

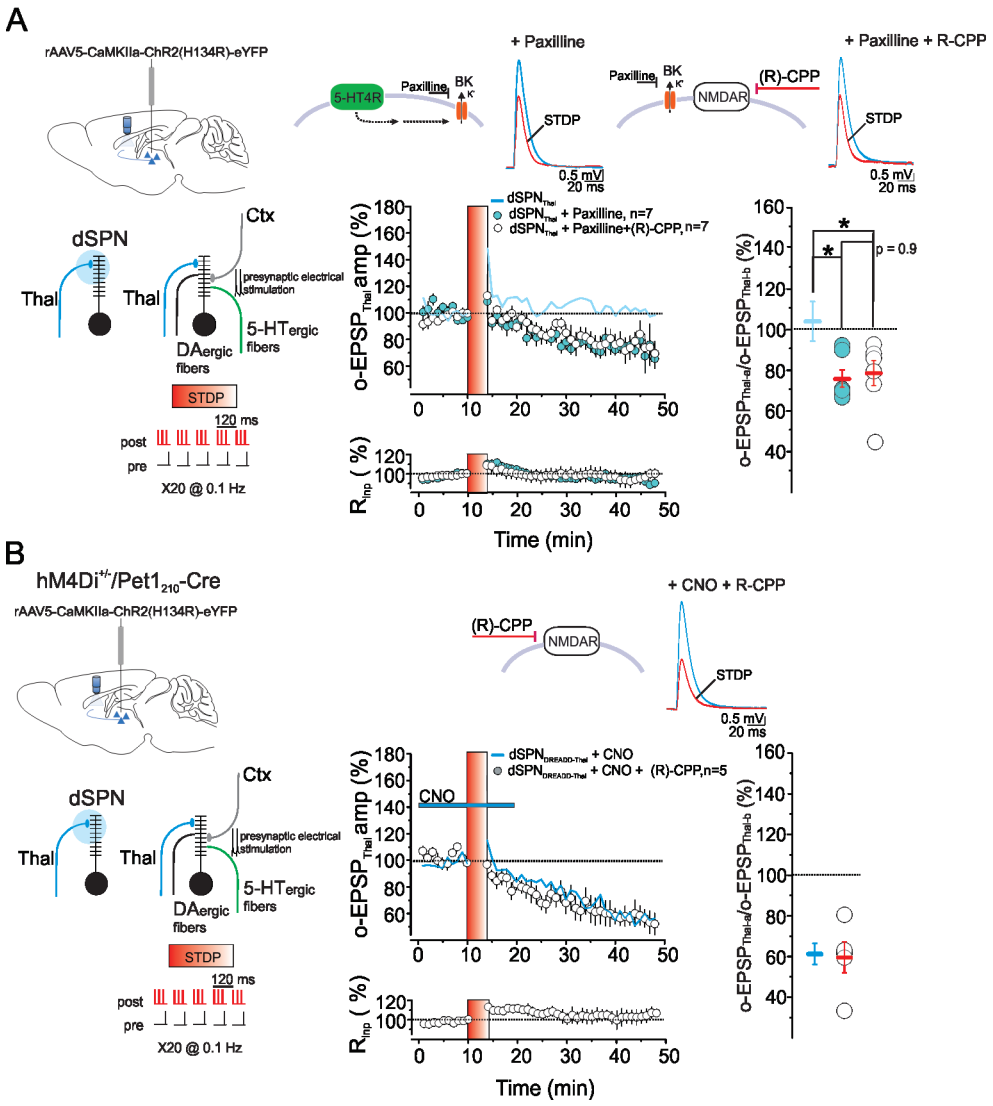

Figure S8, related to Figure 4. BK channels, but not NMDARs, are involved in the 5-HT-mediated regulation of t-LTD at thalamo-dSPN synapses.

(**A**) (Left) Schematic of recording configuration of o-EPSP$_{Thal}$ and during the delivery of the conventional STDP paradigm. (Right) Application of the BK channel blocker paxilline (10 μM) during the STDP paradigm is sufficient to gate t-LTD at thalamo-dSPN synapses (n = 7, 6 mice; RM1WA, $F_{6,44} = 9$, $p = 0.0002$, $p < 0.05$ Tukey), which was not blocked by the NMDAR antagonist R-CPP (10 μM) (n = 7, 2 mice; RM1WA, $F_{6,44} = 3$, $p < 0.0001$, $p < 0.05$ Tukey; 1WA, $F_{2,17} = 5$, $p = 0.02$; dSPN$_{Thal}$ + paxilline versus dSPN$_{Thal}$, *$p < 0.05$; dSPN$_{Thal}$ + paxilline versus dSPN$_{Thal}$ + paxilline + R-CPP, $p = 0.9$; dSPN$_{Thal}$ versus dSPN$_{Thal}$ + paxilline + R-CPP, *$p < 0.05$; Tukey). Solid light blue line (average) is the time-course from **Figure 4E**, reported here for comparison. (**B**) (Left) Schematic of recording configuration of o-EPSP$_{Thal}$ in hM4Di$^{+/-}$/Pet1$_{210}$-Cre mice. NMDAR antagonism does not affect t-LTD gated by CNO application (n = 5, 2 mice; dSPN$_{DREADD_Thal}$ + CNO + R-CPP, RM1WA $F_{4,44} = 14$, $p = 0.0007$, $p < 0.05$ Tukey; dSPN$_{DREADD_Thal}$ + CNO + R-CPP versus dSPN$_{DREADD_Thal}$ + CNO, $p = 0.9$, Mann-Whitney test). Solid light blue line (average) is the time-course from **Figure 4F**, reported here for comparison. (**A-B**) (Left) Data are shown as time courses (mean ± s.e.m.) of normalized EPSP amplitudes and normalized Rinp. (Right) Scatterplot summarizes the ratios of synaptic responses after (a) and before (b) conventional STDP. (Insets) Averaged recordings (ten traces) before (blue line) and after (red line) the delivery the conventional STDP protocol (red vertical bar); schematic represents the proposed signaling pathway and ion channel targeted by the defined blockers (paxilline or R-CPP).

Figure S9

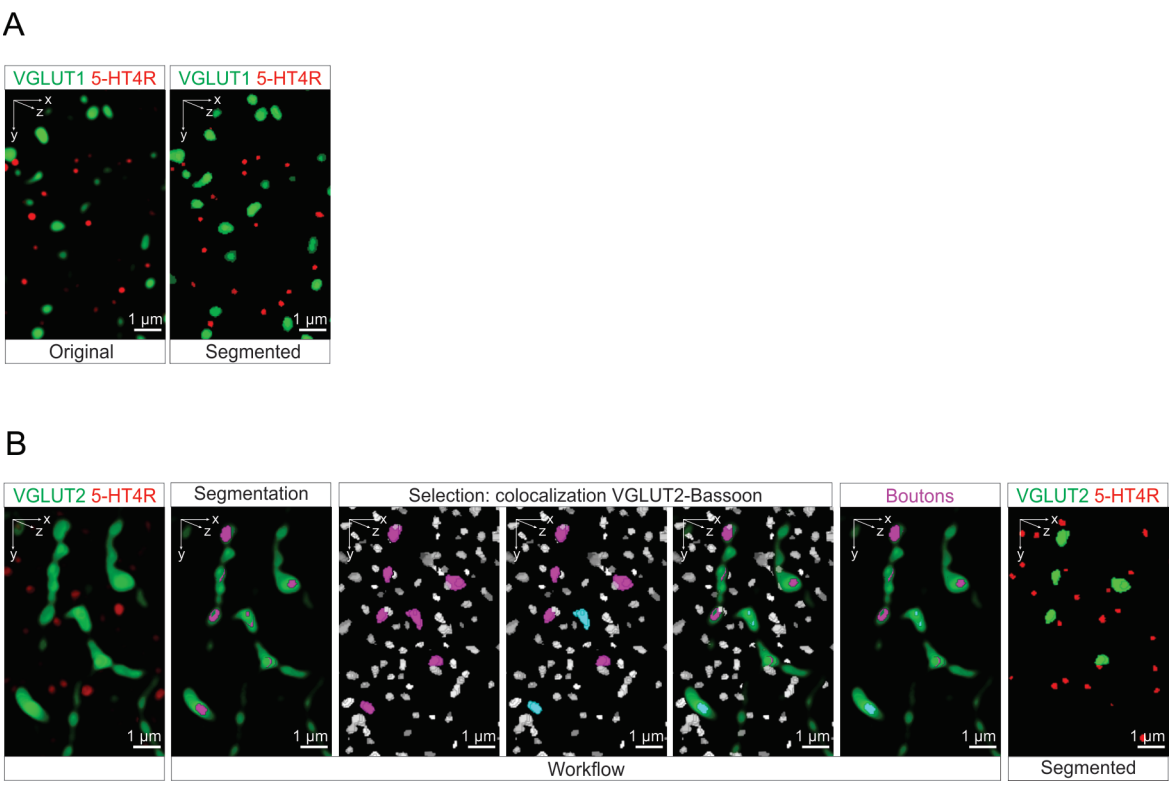

Figure S9, related to Figure 5. 3D volume rendering of postsynaptic localization of 5-HT4R

All images are 3D volume renderings of confocal image stacks illustrating the segmentation workflow that allowed 3D border-to-border measurements and co-localization analysis for 5-HT4R and cortical VGLUT1 and thalamic VGLUT2 boutons in DLS. (**A**) (Left) Immunostaining of 5-HT4R in the DLS of VGLUT1-Venus mice, in which VGLUT1 is fused to Venus and expressed under the endogenous VGLUT1 promoter, allowing direct visualization of cortical presynaptic boutons. (Right) Segmented image with 5-HT4R and VGLUT1 boutons. (**B**) Immunostaining of 5-HT4R in the DLS of VGLUT2-Cre mice after injection of AAV9-FLEX-eGFP in the thalamus, which labels thalamic VGLUT2 afferents. It was combined with immunostaining of presynaptic active zone Bassoon to select the VGLUT2 presynaptic boutons. From left to right: immunostained 5-HT4R with thalamic afferents; the segmentation of eGFP signal (green), retrieved boutons, and axonal segments (purple); segmented eGFP signal (purple) and segmented Bassoon-positive active zones (white); co-localization analysis between Bassoon (white) and segmented eGFP signal allowed to identified Bassoon-positive VGLUT2 boutons (purple) and Bassoon-negative thalamic axonal segments (cyan); eGFP signal (green) with segmented Bassoon (white), selected VGLUT2 boutons (purple) and axonal segments (cyan); eGFP signal (green) with selected VGLUT2 boutons (purple) and axonal segments (cyan); segmented image with 5-HT4R and selected VGLUT2 boutons. (A-B), scale bars, 1 µm).